Electrostatic and Piezoelectric MEMS Scanner Development for Laser Displays

by

Utku Baran

A Thesis Submitted to the
Graduate School of Sciences and Engineering
in Partial Fulfillment of the Requirements for
the Degree of

Master of Science

in

Electrical Engineering

Koç University

July 2012

Koç University
Graduate School of Sciences and Engineering

This is to certify that I have examined this copy of a master's thesis by

Utku Baran

and have found that it is complete and satisfactory in all respects,
and that any and all revisions required by the final
examining committee have been made.

Committee Members:

Dr. Hakan Ürey, (Advisor)

Dr. Erdem Alaca

Dr. Arda Deniz Yalçınkaya

Date: 19.07.2012

ABSTRACT

Laser based displays have been under development over the last 50 years but commercial viability of the technology was limited mainly due to the large size and high cost of laser sources and scanners. The quest for miniaturization and higher efficiency is realized with the development of directly modulatable laser diodes and scanning mirrors based on micro electro mechanical systems (MEMS) technology. Integration of scanners and laser diodes offers a powerful combination for micro-display and imaging applications such as laser printers, barcode readers, and wearable micro-display systems.

A displayed image is formed pixel by pixel using a mirror producing angular motion that scans a modulated light beam on a screen. The purpose of this thesis is to develop new MEMS two dimensional raster scanners for laser display applications.

For the slow axis of the two-mirror display engine, an electrostatically actuated rotary scanner is conceived and developed to provide a linear ramp scan at 60 Hz. A novel spring design is proposed for linear in-plane rotary MEMS scanner. It offers over 98% linear motion up to 7 deg. mechanical rotation with the novel suspension design.

For the fast axis, piezoelectric actuation that requires much lower voltages than electrostatic actuation is used to develop a high frequency resonant torsional MEMS scanner. Sinusoidal actuation with 24 V at a mechanical resonance frequency of 40 kHz provides a total optical scan angle of 38.5 deg. for the 1.4 mm wide mirror. It exceeds the performance specifications cited in the current literature and becomes a significant step towards achieving Full HD (1080p) resolution with mobile laser projectors.

Keywords: Rotary stage, MEMS scanner, Comb-actuator, PZT thin film actuator, Finite-element-modeling, Laser Display.

ÖZET

Lazer tabanlı ekranlar son 50 yıldır geliştirilmektedir ancak lazer kaynaklarının ve tarayıcıların çok yer kaplaması ve yüksek maliyeti nedeniyle ticari uygulanabilirliği sınırlı kalmıştır. Mikro Elektromekanik Sistem (MEMS) teknolojisi ile üretilen mikro tarayıcılar ve doğrudan kontrol edilebilen lazer diyotların gelişimi ile küçük ve verimli lazer tabanlı ekranlar üretilmeye başladı. Mikro tarayıcılar ve kontrol edilebilen lazer diyotların birlikteliği ile lazer yazıcılar, barkot okuyucular ve giyilebilir mikro-görüntüleme sistemleri gibi ticari uygulamalar geliştirilmiştir.

Bu teknolojiyle üretilen mikro görüntüleme sistemlerinde ekrandaki görüntü doğru renkte ayarlanmış ışık demetini iki eksende dönen bir ayna yardımıyla piksel piksel tarayarak oluşur. Bu çalışmanın amacı, lazer tabanlı mikro görüntüleme uygulamaları için iki eksende kullanılacak yeni MEMS tarayıcılar geliştirmektir.

İki aynalı görüntü motorunun yavaş tarama ekseninde çalışan aynası için, tarak tahrikli dönen bir yapı, modellenip, üretilmiş ve 60 Hz frekansında doğrusal tarama sağlamak için kullanılabileceği ortaya konmuştur. Bu tarayıcıyla birlikte, tarak tahrikli düzlemsel dönen MEMS yapılarda kullanılmak üzere doğrusal hareket sağlayan yeni bir süspansiyon tasarımı geliştirilmiştir. Yeni süspansiyon tasarımı 7 derece mekanik dönme açısına kadar % 98'in üzerinde doğrusal hareket imkânı sunmaktadır.

Hızlı tarama ekseni için ise ince film PZT ile çalıştırılan yüksek frekanslı tınlaşım mikro-tarayıcı geliştirilmiştir. 1.4 mm genişliğinde aynası olan bu tarayıcı 40 kHz mekanik tınlaşım frekansında 24 V sinüs ile sürüldüğünde toplam 38.5 derece optik tarama açısı sağlamaktadır. Bu performansıyla güncel kaynakçadaki eşlenikleriyle kıyaslandığında dünyada liderdir ve mikro görüntüleme sistemleri ile 1080p çözünürlüğe ulaşma yolunda önemli bir adımdır.

ACKNOWLEDGEMENT

I am grateful to Prof. Hakan Ürey for being my primary mentor since my sophomore year at Koç University and guiding me into several exciting projects in OML. I am also thankful to Prof. Erdem Alaca and Prof. Arda Deniz Yalçınkaya for taking a part in my thesis committee.

It was a privilege to work with world-class engineers Dean Brown, Wyatt Davis, and Mark Helsel from Microvision Inc. who helped me develop a solid background in MEMS engineering during my graduate studies. I am in debt to Dean for answering my questions whenever I was in trouble with ANSYS and always encouraging me in the teleconferences. Wyatt is one of the greatest people I have met as a researcher. In addition to his valuable knowledge he shared during our meetings, I am also grateful to him for introducing me to several top-notch Professors in the US without any reservations for my Phd. applications. I want to thank Mark for sharing his experience in MEMS fabrication during our meetings and his hospitality during my 2011 stay in Seattle.

I am thankful to Sven for his highly valuable partnership as well as for our enjoyable conversations. Onur Ferhanoğlu is one of the greatest people on Earth and I feel lucky to know him since my undergraduate years. Kutal has always been a trusted friend and a knowledgeable colleague. I am thankful to Kaan for his company in all the weekends spent at the office and sharing his knowledge on programming and space travel.

I have had the pleasure of working with many colleagues in 5 years at OML, but I really enjoyed being in a group with Erhan, Selim, Ulaş, Onur Çakmak, Başar, Kıvanç, Zeynep, Cem, Burak and Dr. Cağlar during my graduate student years.

Last but not least, I am deeply grateful to my family for doubtlessly believing in me, and my sweetheart Kardelen for her understanding and support in all the dark times.

Dedicated to my dear mother,

LIST OF FIGURES

LIST OF TABLES

Table of Contents

1 OVERVIEW OF MEMS SCANNERS FOR LASER DISPLAYS

Laser based displays have been under development over the last 50 years but commercial viability of the technology was limited mainly due to the large size and high cost of laser sources. The quest for miniaturization and higher efficiency replaced the modulators and scanning technologies in this type of projectors with directly modulatable laser sources and scanning mirrors based on micro electro mechanical systems (MEMS) technology, respectively.

Even though the idea of using lasers for displays was proposed in the 1960's [1], it is the availability of lasers emitting red, green and blue colors triggered the recent development of portable laser projectors. An immediate advantage of using spectrally pure laser light for displays is the wide color gamut it can produce [2]. Integration of scanners and laser diodes provide a powerful combination for a wide array of applications for MEMS scanners, including barcode readers, quality inspection, printing, information handling, surveillance, medical imaging and several types of displays.

MEMS laser scanner compete with liquid crystal on silicon (LCoS) [3] and digital light processing (DLP) based microdisplays for mobile projector applications [4]. LCoS based systems use red, green and blue light emitted diodes (LED) [3] or laser diodes [5] as light source. Its working principle is very similar to liquid crystal display (LCD), but it has a size advantage due to no need for color filters [3]. On the other hand, DLP projectors use digital micro-mirror device (DMD) and LEDs as light source with additional optics. It can be as compact as 2.1 cc (20.6×16.4×6.2 mm) and it offers better optical efficiency and contrast ratio [6].

This chapter is focused on MEMS laser scanners for mobile displays and the comparisons made accordingly. However, the same scanners can also be used for heads-up-displays, head-mounted displays, or imaging applications. The aim has also been to be as inclusive as possible regarding operation principles and approaches to light beam scanning e.g. imaging and displays, but then focus more on the scanner architectures which have produced high performing scanners.

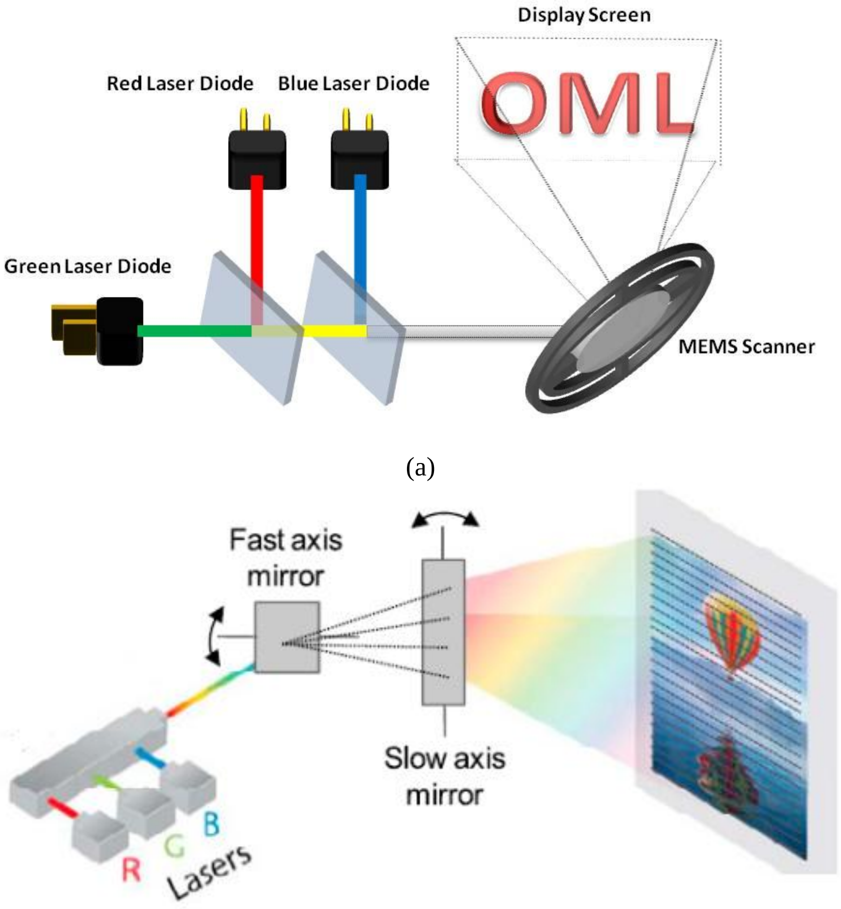

(a)

(b)

Figure 1.1 Schematic of a flying spot laser projector. (a) Configuration with 2D scanning mirror (b) Configuration with two unidirectional mirror [7].

The majority of high performing display scanners are of the rotating mirror type where a mirror producing angular motion is used to deflect a modulated light beam on an image plane to create a display as illustrated in Fig 1.1 To create the proper color mix for each pixel, all lasers are modulated simultaneously. Direct modulation of the lasers for each pixel facilitates good power efficiency and inherently high contrast [8]. The efficiency is maximized, since the lasers emit only at the level needed for each pixel. The contrast is high because the lasers are completely off for black pixels. This efficiency and contrast advantages are not present in spatial light modulator based displays where excess intensity is deflected or absorbed. Moreover, since there is no projection lens in the system, the image size and the spot size both scale linearly with the distance from the projector, thus, the number of resolvable pixels remain the same and the image always remain in focus.

In order to construct a two-dimensional (2-D) raster-like rectangular image, two-axes-scanning at different frequencies is required. This requirement can be satisfied either with a single 2D scanning mirror [9] or two-mirror architecture where each mirror is responsible for one axis [7] as shown in Fig. 1.1.

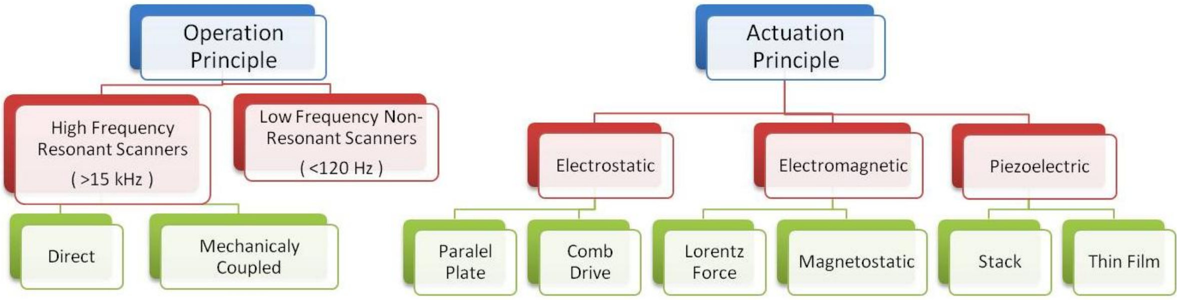

Figure 1.2 Typical classification of MEMS Laser Scanners for Mobile Displays.

Providing a fast and compact actuator to meet the actuation force requirements at reasonable voltage and power levels is an important challenge for the system design. The scan frequency has to be high enough to handle the millions of pixels per second, and the scan angle has to be large in order to paint a wide angle, 2-D image.

The typical MEMS laser scanners with rotating mirror used in modern display systems are classified as in Fig. 2. Different actuation methods and drive mechanisms have been heavily researched over last decade to address the requirements of MEMS scanners for mobile displays. Each technology has its own drawbacks and advantages over its counterparts. In this chapter, today's technology alternatives of MEMS Scanners for mobile display applications is summarized including a comprehensive comparison, and provided a road map for the future challenges of each technology.

1.1 Requirements for MEMS Laser Scanner Displays

Image quality of the MEMS scanner based laser displays depends on multiple figures of merit. The resolution of the display is determined by $\theta \cdot D \cdot f_h$ product, where θ is the scan angle, D is the diameter of the scanning mirror, and f_h is the horizontal scan frequency. Moreover, the refresh rate of the display translates into f_v, the vertical scanner frequency. The ratio of horizontal scan frequency to display refresh rate determines the vertical display lines [9].

The number of resolvable spots in the horizontal direction can be rewritten in terms of the total optical scan angle (TOSA), θ_{opt}, the mechanical zero-to-peak angle θ_{mech}, and the mirror diameter D according to [10, 11]

$$\mathrm{N} = \frac{\theta_{\mathrm{opt}} D}{a\lambda} = \frac{4\theta_{\mathrm{mech}} D}{a\lambda} \tag{1-1}$$

where, λ is the optical wavelength, and *a* is a shape factor determined by various aperture shapes and illumination conditions which can take values from 0.75 to 2 or more depending on the definition of spot size, the aperture shape, and Gaussian beam clipping at the system apertures [10].

In order to reduce the frequency burden of the scanner and improve the duty cycle of the light sources, bidirectional writing scheme can be used. Bidirectional writing refers to displaying a new line of data in both scan directions while unidirectional writing presents data only during the forward sweep of the horizontal scanner. Bidirectional writing scheme let the scanner to write two lines during one scan cycle, and hence increases the light source utilization by a factor of 2 and reduces the required horizontal scanner frequency by half [11]. Although unidirectional writing scheme can provide better line to line positional uniformity, bidirectional writing with a high frequency resonant horizontal “fast axis” and a non-resonant linear ramp “slow axis” appeared as the preferred system architecture [12].

	VGA	**WVGA**	**SVGA**	**HD720p**	**HD1080p**
Horizontal Resolution	640	854	800	1280	1920
Vertical Resolution	480	480	600	720	1080
θ·D product (deg mm)	**7.8**	**9.7**	**9.7**	**11**	**23.3**
f_h (kHz)	**18**	**18**	**20**	**28**	**42**

Table 1.1 θ·D and horizontal frequency requirements of various resolutions for displays using bidirectional ramp scanning architecture.

There are also additional factors to be considered while calculating the required θ·D product: beam profile across the scanner, operation wavelength, usable portion of the scan line, static and dynamic flatness of the mirror surface, and clear aperture size of the mirror. Furthermore, mechanical reliability of the scanner and accuracy of scanner position information from position sensors are the other important factors. Detailed information about optical performance requirements is presented in [11]. Tab. 1.1 above shows θ·D and horizontal frequency requirements needed to address various image resolutions of a bidirectional ramp scanning system at a 60Hz refresh rate [11, 12].

1.2 Actuation Principles

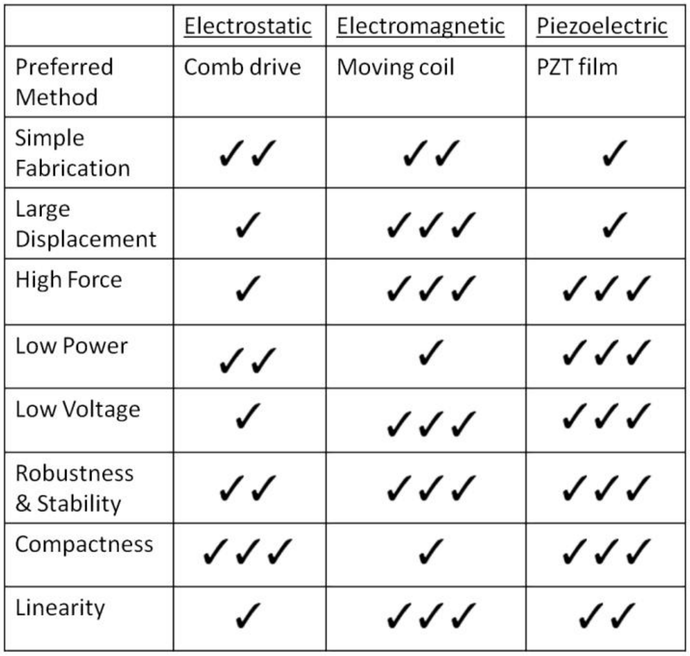

	Electrostatic	Electromagnetic	Piezoelectric
Preferred Method	Comb drive	Moving coil	PZT film
Simple Fabrication	✓✓	✓✓	✓
Large Displacement	✓	✓✓✓	✓
High Force	✓	✓✓✓	✓✓✓
Low Power	✓✓	✓	✓✓✓
Low Voltage	✓	✓✓✓	✓✓✓
Robustness & Stability	✓✓	✓✓✓	✓✓✓
Compactness	✓✓✓	✓	✓✓✓
Linearity	✓	✓✓✓	✓✓

Table 1.2 θ·D and horizontal frequency requirements of various resolutions for displays using bidirectional ramp scanning architecture.

For laser display applications, large mirror and displacement are required, and these requirements lead various problems to overcome for both horizontal and vertical scans. For the horizontal (high frequency) scan, a high drive torque is required to operate at atmospheric pressure that produces high damping. Moreover, the non-resonant operation of the vertical scan demands a high torque to overcome the flexure stiffness. This stiffness cannot be set very low due to requirements for shock and handling robustness. The suspended mass becomes heavy due to large mirror size and dynamic flatness requirements [13].

The most critical aspects to consider when comparing scanners for commercial use are: fabrication simplicity, power efficiency, low voltage requirement, robustness, compactness, and long-term stability. Each actuation principle has advantages on some aspects while having disadvantages on others. When comparing the electrical performance of the actuation principles, mechanical performance is fixed. Tab. 1.2 above compares the properties of each actuation principle according to their use in MEMS laser scanners for mobile displays.

1.2.1 Electrostatic Actuation

Electrostatic actuation has been the most favorable actuation method since the early years of MEMS. Its fabrication is inherently compatible with techniques developed for microelectronics technologies whereas other actuation schemes required new machines and techniques to become available for MEMS.

Working principle of electrostatic actuation relies on the attraction of two oppositely charged plates. There are two main concepts of electrostatic actuation: comb actuation and parallel-plate actuation. Comb actuation is a frequently used concept for MEMS laser scanners. In this concept, multiple plates are attached to each other like comb fingers to constitute a comb actuator. Moreover, parallel-plate actuation is used in some applications like DMD based projectors [4], where each mirror is switched on/off by creating a voltage difference on one side of the parallel-plate actuator. However, it is not as popular as comb actuation for MEMS laser scanners.

Electrostatic actuation provides CMOS compatible fabrication, long-term stability, and compact size advantages. On the other hand, it requires high voltages to operate, and tends to lack robust operation due to "pull-in" phenomenon. Particularly comb actuation is prone to fail over a large travel due to this phenomenon related to an interaction of a nonlinear electrostatic force with a linear elastic restoring force [14].

1.2.2 Electromagnetic Actuation

Electromagnetic actuation is a strong alternative to fulfill the requirements of MEMS laser scanners. After the necessary fabrication techniques have been developed for electromagnetic actuation, it became a popular method for MEMS laser scanner actuation.

There are two major working schemes in use. The first scheme is called Lorentz force excitation and it consists of a coil fabricated on a device and external magnets to provide static magnetic field as illustrated below in Fig. 1.3. On the contrary, second scheme is called magnetostatic actuation and uses an external coil and thin magnetic film deposited on device. It eliminates the need of wire bonds since the actuation is driven with an off-chip coil.

A magnetic drive produces the necessary high torques over large scan angles. However, usage of a coil and a magnet for the MEMS laser scanner actuation brings certain disadvantages. Firstly, achievable performance of the electromagnetically actuated MEMS scanner is limited with a large thermal dissipation of coil. High conducting currents inside a coil also consume significant power that diminishes the battery life of portable displays. Additionally, bulky magnets take up a significant space and require magnetic shielding that lead to a large device size.

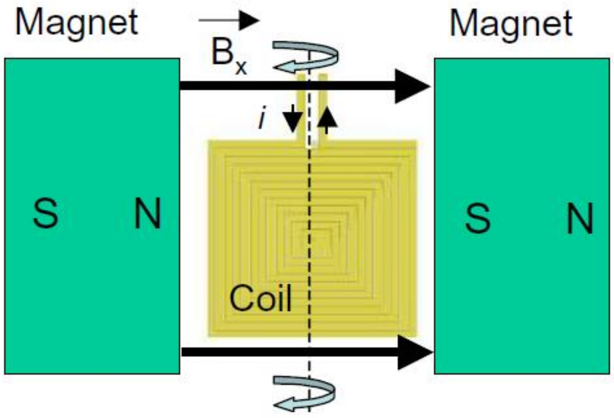

Figure 1.3 General configuration of a Lorentz force excited torsional scanner with coils and magnets [15].

1.2.3 Piezoelectric Actuation

Piezoelectric actuation had not been used in MEMS laser scanners as often compared to other methods due to the lack of convenient fabrication techniques and machinery, although it provides several advantages over other methods [16]. When reliable and convenient fabrication techniques were developed for thin film deposition of piezoelectric materials, it has taken attention as a major actuation principle for MEMS laser scanners in the last decade. On the other hand, stack piezoelectric actuators have not been as favourable due to the difficulties in monolithic fabrication via the silicon wafer process and its large size.

The first attempts to fabricate piezoelectric actuated MEMS have been undertaken with thin film materials such as ZnO and AIN. Although they are easier to deposit, a lead zirconate titanate (PZT) film of equal thickness develops ten times larger forces [17]. Hence, PZT is the most popular material used for MEMS scanner actuation.

Piezoelectric actuation with thin-film PZT offers equal performance at much lower voltage levels than ES scanners and has a higher energy efficiency [16] and much smaller package size compared to EM scanners. Moreover, piezoelectric actuators can measure deflection from the piezoelectric voltage of the separated electrode [18] or the piezoelectric current charge [19]. Thus, they can be used as angle sensors for closed-loop control of micro scanners without any additional process or material. It also generates no electromagnetic noise, so it does not require any magnetic shielding to be used in commercial products unlike EM actuators. On the other hand, limited deflection of PZT beams is a major problem when large angles are needed for high-resolution displays.

1.3 Resonant Scanners (Fast Axis)

1.3.1 Electromagnetically Actuated Scanners

As stated earlier, high power consumption is a major problem for electromagnetically actuated high frequency resonant scanners at large angles. Increased heat generation with large currents decreases power efficiency, which reduces the battery life of a portable device. Hence, it is a challenging task to develop electromagnetically actuated high frequency MEMS scanners with low power consumption.

Early work of Miyajima et.al [20] presented a large $5\times3.7\ \text{mm}^2$ mirror with a rotation of ±8.4° optical scan angle in resonance at 2.7 kHz which is not suitable for micro displays. It requires around 350 mA current with Lorentz force excitation.

Raboud et.al [7] reported one of the few 1D electromagnetically actuated resonant MEMS laser scanners for micro displays in the current literature. In this work, 1mm mirror, which is a part of the two mirror scan architecture, can be rotated ±20° optical scan angle in resonance at 19.5 kHz with Lorentz force excitation. Moreover, Reyne [21] developed magnetostatic actuated 20 kHz resonance frequency MEMS laser scanner with 2×4 mm^2 mirror that can rotate up to 5 deg. optical scan angle. Power consumptions of the scanners are not reported.

Majority of the reported electromagnetically actuated MEMS laser scanners offer either non-resonant 1D scan or 2D scan which will be covered in Section 1.4.1 and Section 1.5.1, respectively.

1.3.2 Electrostatically Actuated Scanners

There has been an intense research on electrostatically actuated MEMS scanners in the last decade [22-27]. For electrostatically actuated resonant MEMS scanners, the performance is typically limited by the damping power losses at high frequencies and the small actuator capacitance of the structure due to limited perimeter area around the torsion mirror. Arslan et.al [26] proposed a mechanical-coupling principle as a solution to overcome these limitations. The mechanically coupled comb-drive systems have two cascaded platforms, as shown in Fig. 1.4, referred to as the inner and outer frames, connected by the inner flexures. Only the outer frame bears the ES comb-drive actuators, and the deflection of the outer frame is coupled to the inner frame. The main intended advantage of this arrangement compared with one without an outer frame (i.e., with the driving comb fingers attached directly to the mirror instead) is a reduced damping on the high velocity mirror rotations. Experimental evidence for significant reductions in air damping of comb-drive scanning mirrors when the comb-finger gaps are increased has been shown in [28]. By removing the fingers completely from the high velocity inner frame and transferring them to a lower velocity outer frame, damping reduction comes to an extreme. In this design, with 1 mm wide mirror, a 76 deg. total optical scan angle is achieved at 21.8 kHz with 196 V peak-to-peak excitation voltage.

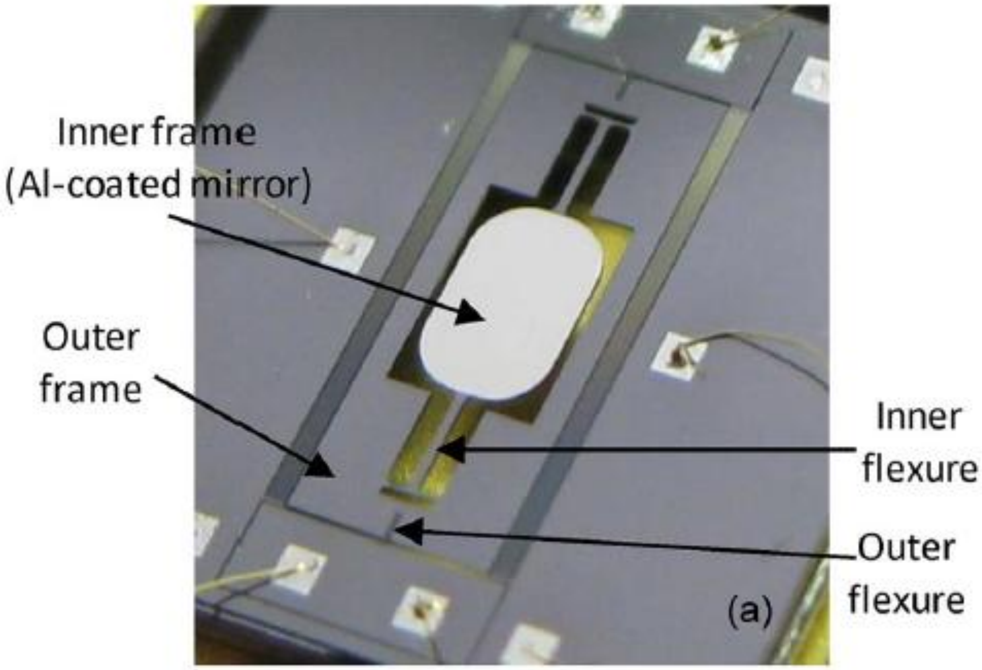

Figure 1.4 Picture of a full die of torsional electrostatic scanner [26].

Moreover, Cho et.al [23] presented scanner that has a long actuator attached to mirror as shown in Fig. 1.5. As a result, mechanical tilting angle of ±12.0 degree was achieved with the resonant frequency of 24.75 kHz and the sinusoidal driving voltage of 280Vpp.

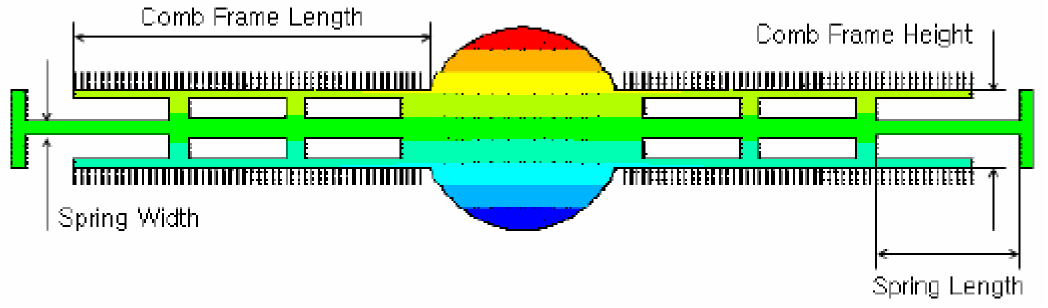

Figure 1.5 Structural design variables used in design optimization of actuation part and torsional bar [23].

1.3.3 Piezoelectric Actuated Scanners

Piezoelectric actuation is a promising actuation method for resonant scanners. Significant research effort has been spent in the last decade to develop such scanners. To achieve large scan angles at high frequencies, damping losses and limited deflection of PZT beams with large stiffness are the two main obstacles to overcome for resonant piezoelectric actuated scanners.

Smits et. al developed one of the first successful piezoelectric thin-film actuated resonant scanners in 2005 [29]. In this work, 1.3 mm mirror can rotate at optical angles of up to ±15° in resonance at 17.4 kHz at driving voltages of around 6 V. Same year, Filhol et. al. also introduced a novel actuator design consists of a silicon membrane and a PZT thin film [30]. As shown in Fig. 1.6, a 500 um circular mirror is asymmetrically (50 um off axis to the center of mass of the mirror) mounted on two lateral torsional hinges linked to the actuators so that the vertical translational excitation is converted into a rotational oscillatory movement of the mirror which can give ±20.4° optical scan angle in resonance at 25.4 kHz with driving voltage of 42 V_{pp}.

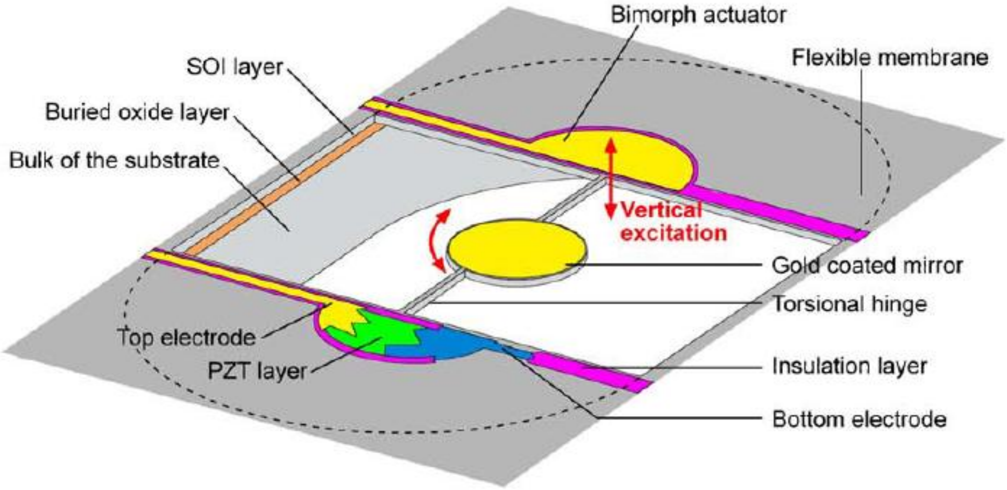

Figure 1.6 Schematic illustration of a design of the PZT actuated microscanner uses a silicon membrane [30].

Metal based piezoelectric MEMS scanners are also investigated. Park et. al. introduced a stainless steel based piezoelectric scanner, where 1 mm mirror rotates ±20.5°optical scan angle at 28.24 kHz resonance with driving voltages of 60 V_{pp} [31]. Moreover, Matsushita et.al developed a PZT thin film actuated scanner on a Ti substrate to simplify the fabrication process of piezoelectric thin film MEMS. At driving voltage of 20 V_{pp}, ±22° optical scan angle in resonance at 25.4 kHz is achieved with 1 mm mirror [32].

There are few examples where stack piezoelectric actuator is used in MEMS laser scanners for displays. Iseki et. al. demonstrated a large rotation of ±27° optical scan angle at 38 kHz with 1 mm mirror using a stack piezoelectric actuator [33].

1.4 Non-Resonant Scanners (Slow-axis)

1.4.1 Electromagnetically Actuated Scanners

Unlike the case with resonant scanners, there are several successful examples of electromagnetically actuated non-resonant MEMS laser scanners. Large force and longer operation range capabilities of EM actuators make them very useful when static displacement is needed.

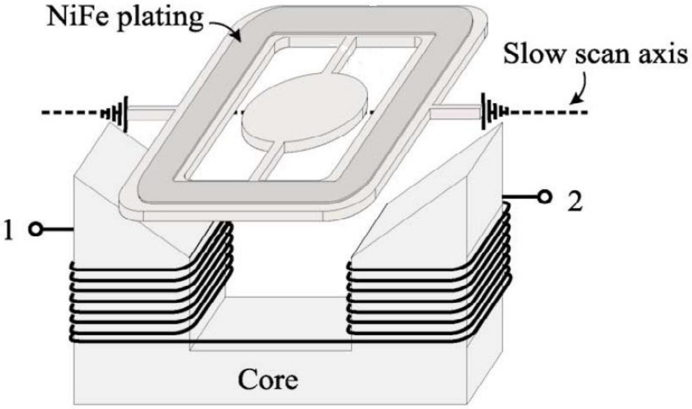

Figure 1.7 Configuration of a microscanner with an external electrocoil and an on-chip NiFe layer [34].

Jeong et.al [35] from Samsung Electrics Company, Ltd. proposed a Lorentz force excited slow scanner that can be used to horizontally scan a vertical line image made through a line-type diffractive spatial optical modulator (SLM). In this design, large 3×1.5 mm^2 mirror can be rotated ±15° optical scan angle with 98% linearity at 120 Hz non-resonant frequency, and it consumes 60 mW power. To minimize the device size and the power consumption, the mirror surface is placed on the front side of the device, whereas coil actuator placed on the bottom side. Moreover, mechanical stoppers are used to make the device shock-proof. Wafer-level packaging is realized using an additional glass wafer, and total size of the package became 9.2 mm×10 mm×3 mm (0.28cc).

Yalcinkaya et.al [34] describes a system that has a similar design to [9]. However, it uses a magnetostatic torque generated by an external electrocoil and an on-chip NiFe layer instead of Lorentz force excitation (Fig. 1.7). In this way, very large angle of static mirror rotation up to ±44° optical scan angle with 1.5 mm mirror is realized. It consumes 170 mW power.

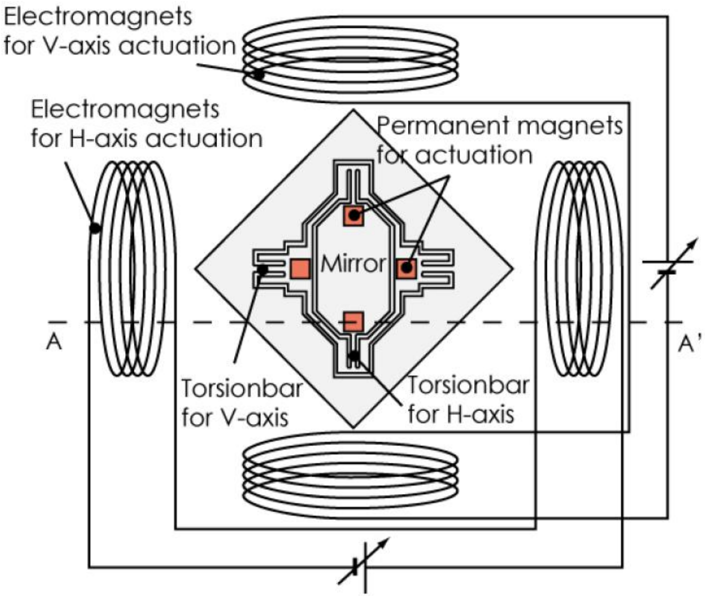

Figure 1.8 Schematic that shows the orientation of permanent magnets and electromagnets with respect to double-gimbal structure [36].

Moreover, Makishi et.al [36] uses magnetostatic actuation to generate very large mirror rotation up to ±59° optical scan angle with static drive. Here, four permanent magnets are attached to a double-gimbal structure and the mirror rotation is realized with four electromagnets as illustrated in Fig. 1.8. The power consumption of the device and the size of the mirror are not reported. The possible unreported problems with this device are poor shock resistance and bulky size. Permanent magnets add comparably large amount of inertia to the double-gimbal structure and makes it easier to break under shock. Furthermore, electromagnets consume large space, which makes the device bulky for mobile displays.

1.4.2 Electrostatically Actuated Scanners

Typical out-of-plane comb scanners for laser beam scanning applications are only suitable for resonant actuation and do not respond to DC [37]. This can be addressed by making off-set comb fingers [38, 39] or by using electrodes on a separate wafer [40].

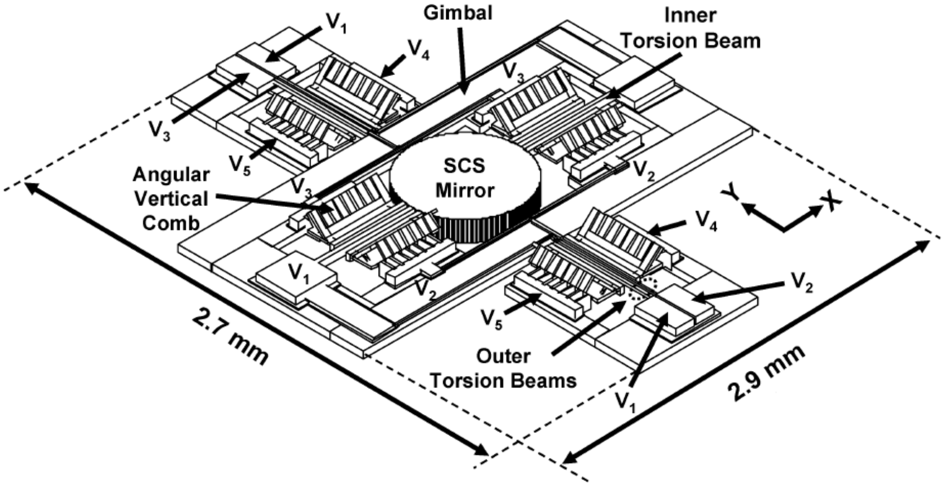

Figure 1.9 Schematic of the 2-D AVC scanner.

Piyawattanametha [38] et.al describes a design where combination of a foundry-based surface-micromachining process with a three-mask deep-reactive ion-etching (DRIE) process is used to realize a 2-D optical scanner with electrostatic angular vertical comb (AVC) actuators. The presented scanner (Fig. 1.9) achieves dc mechanical scanning ranges of ±6.2 deg. (at 55 V_{dc}) and ±4.1 deg. (at 50 Vdc) for the inner and outer gimbals, respectively.

Moreover, Milanovic et.al [41] developed a gimbal-less micromirror (Fig. 1.10) that is actuated by four orthogonally arranged vertical comb-drive rotators etched in the device layer of a silicon-on-insulator wafer, which are coupled by mechanical linkages and mechanical rotation transformers to a central micromirror. One-axis micromirror achieves static optical scan angle of >20 deg. at <150 V operation.

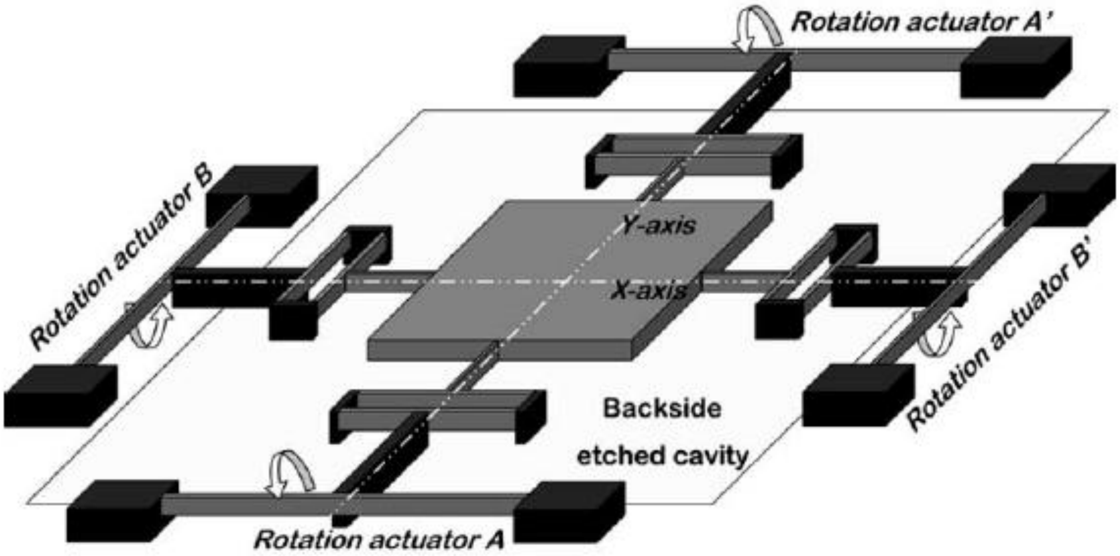

Figure 1.10 Schematic of the scanner operation. Device consists of four vertical comb-drive rotation actuators, here shown just as torsion beams working in pairs to provide each of two axes of rotation [41].

As an alternative, in-plane rotation using curved comb fingers can also be used as resonant scanning platform for laser scanning applications [42], but in-plane MEMS scanners are affected by the nonlinear spring stiffening of suspension beams used in bending mode rather than torsion mode. Hence, there are few examples of in-plane MEMS scanners that provide linear ramp motion for the slow axis of laser displays [43].

1.4.3 Piezoelectric Actuated Scanners

Limited static displacement capability of piezoelectric actuation is a major problem for non-resonant MEMS scanners. Thus, it is a challenging task to develop a piezoelectric actuated non-resonant MEMS scanner for mobile displays.

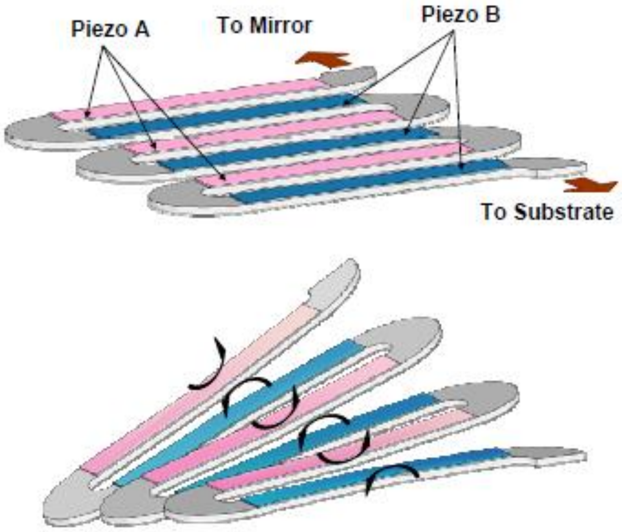

Figure 1.11 Mechanism of the accumulating angular displacement of piezoelectric cantilever formed in a meandering shape. Upward and downward displacements sum up to a large deflection at the tip [44].

Tani et.al introduced a solution to overcome the limited deflection of piezoelectric actuated beams [44, 45]. In this design, large static deflection up to ±8.6° mechanical angle at an applied voltage of 20 V_{dc} is achieved by accumulating angular displacement in a cascaded piezoelectric cantilever formed in a meandering shape as illustrated in Fig. 1.11.

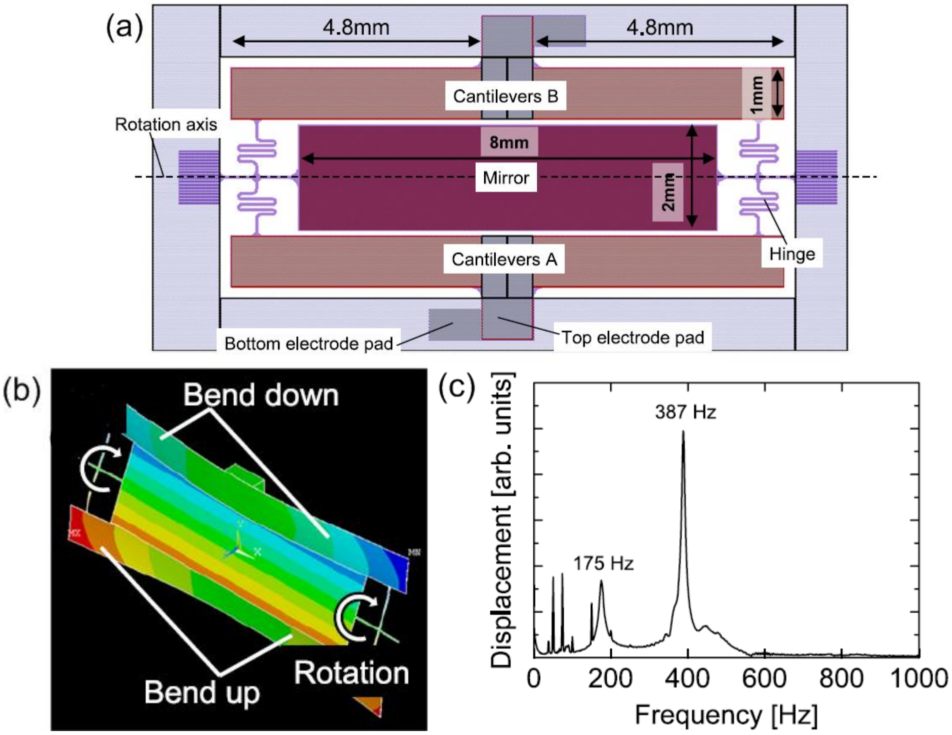

Figure 1.12 Schematic illustrations of (a) design and dimension of the present microscanner. b) Illustration of the desired working scheme. c) Frequency response of the microscanner. [46]

It is known that meandering type cantilevers create many irrelevant modes at low frequencies. Non-resonant operation of scanner for displays demands high precision in motion. Harmonics of the irrelevant modes close to the operation frequency may disturb the motion of the mirror. Although large static deflection angles can be achieved with meandering type cantilevers, the mode separation arises as a problem at low frequencies.

Moreover, Kobayashi et.al [46] used long cantilevers to create large angle rotation of a mirror (Fig 1.12). In this way, ±5.3° mechanical angle at an applied voltage of 10 V_{dc} is achieved. However, it again suffers from the poor mode separation problem. As shown in Fig. 1.12c, there are many irrelevant modes very close to the working frequency, which is typically 60 Hz.

1.5 2D Scanners

1.5.1 Electromagnetically Actuated Scanners

Electromagnetic actuation is used for MEMS laser scanners that are core components of commercially available mobile projectors [7, 12]. Microvision Inc. has been utilizing Lorentz force excited 2D MEMS scanners as an engine for their NOMAD head-worn displays and PicoP mobile projectors [9, 12, 13]. Early designs required a vacuum package, which significantly increases the package size and the cost, to achieve a desirable performance. In 2005, new bi-axial magnetic drive scheme made a breakthrough in performance so that the need for a vacuum package is ironed out [13]. In this scheme, superimpose of the drive torques, which are applied at 45° relative to the two scan axes are used for the scan in both vertical and horizontal directions as illustrated in Fig. 1.13. The frequency components of the applied torque are 20 kHz for the horizontal resonant motion and 60 Hz for the vertical non-resonant ramp motion. Using single coil and single magnet for excitation of a 2D scan profile makes drive scheme simple and power efficient.

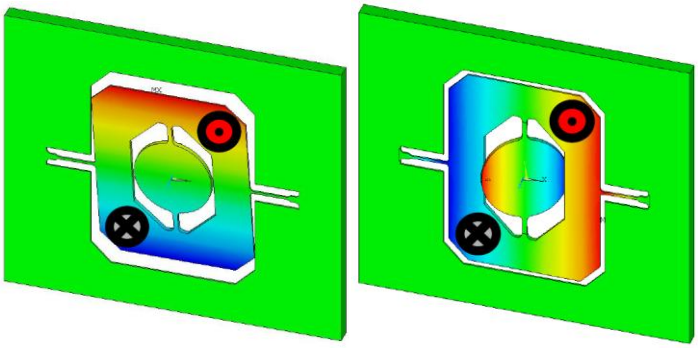

Figure 1.13 Superimposed torque drives for vertical (on the left) and horizontal (on the right) axes of mirror motion [13].

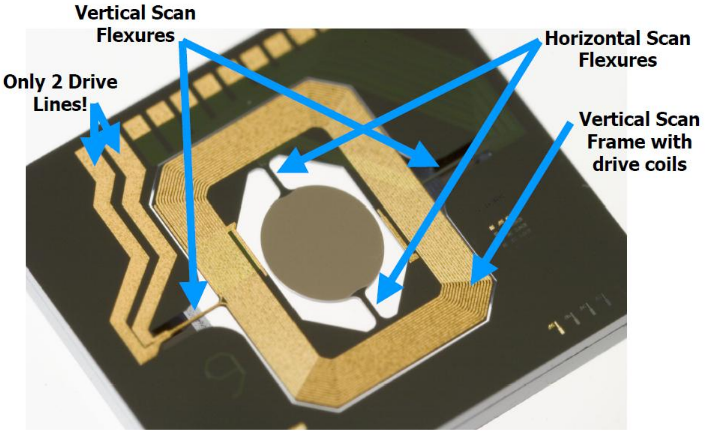

Figure 1.14 Features of the Bi-Axial Magnetic Drive [13].

Yalcinkaya et.al [9] published a 2D MEMS scanner that uses the same design features shown in Fig. 1.14. In this work, 1.5 mm mirror, with 140 mA current, can rotate up to ±26.5° and ±33.5° optical scan angles for resonant horizontal scan at 21.3 kHz and non-resonant vertical scan at 60 Hz, respectively. For the resonant scan, out-of-phase mode is used to benefit from mechanical coupling. With these figures, it is capable of supporting SXGA displays.

Ji et.al [47] presented a scanner that again uses the mechanical coupling principle for resonant scanning but it utilizes a single turn coil and radial magnetic field from concentric magnet assembly rather than using a multi turn coil and lateral magnetic field oriented 45° to the scan axes to achieve a bi-axial magnetic actuation (Fig. 1.15). A single turn coil is easier to fabricate than a multi turn coil. A concentric magnet assembly, composed of cylindrical and annular magnets and an iron yoke, provides larger radial magnetic field compared against the conventional magnets. In this design, 1.5 mm mirror operating with 131 mA current produces ±4.4° and ±4.2° optical scan angles in resonance operation at 19.1 kHz, and in static mode operation at 60 Hz, respectively.

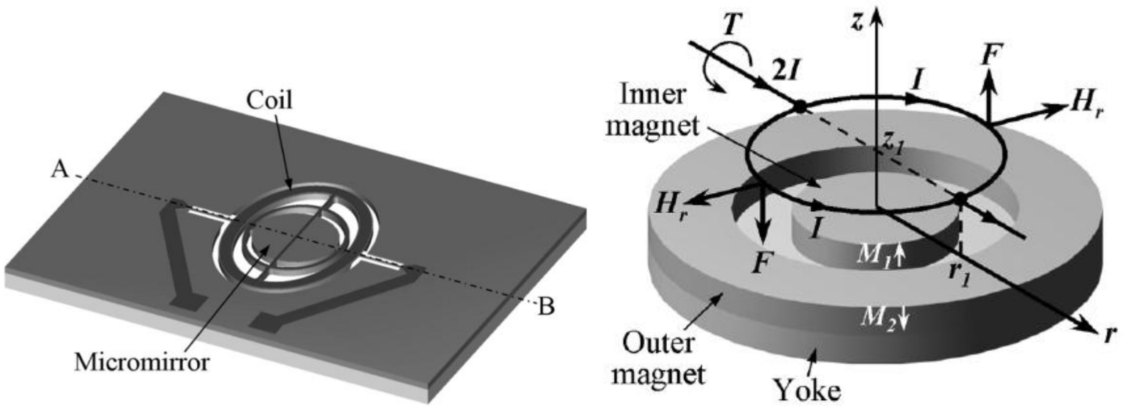

(a) (b)

Figure 1.15 (a) A schematic view of the scanning micromirror. (b) Schematics of the coil and concentric magnet assembly (M: magnetization, F: force, T: torque, H: magnetic field intensity, I: current) [47].

1.5.2 Electrostatically Actuated Scanners

2D electrostatically actuated microscanner is a good candidate for serving in a hand-held laser projector. Fraunhofer Institute for Photonic Microsystems (FhG-IPMS) has been developing electrostatically actuated MEMS scanners for more than 10 years [37, 48, 49]. In early works, resonant mode operation for both axes are used in 2D scanners developed by IPMS [50]. In these designs, resonance frequency ratios of the fast and slow axes should be high. However, the double resonant actuation principle has some limitations. When it comes to HD displays, linear scanning has less impact on the dynamic deformation of the mirror compared to Lissajous scanning because of the lower scan frequencies. Double resonant actuation also demands larger electronic bandwidth.

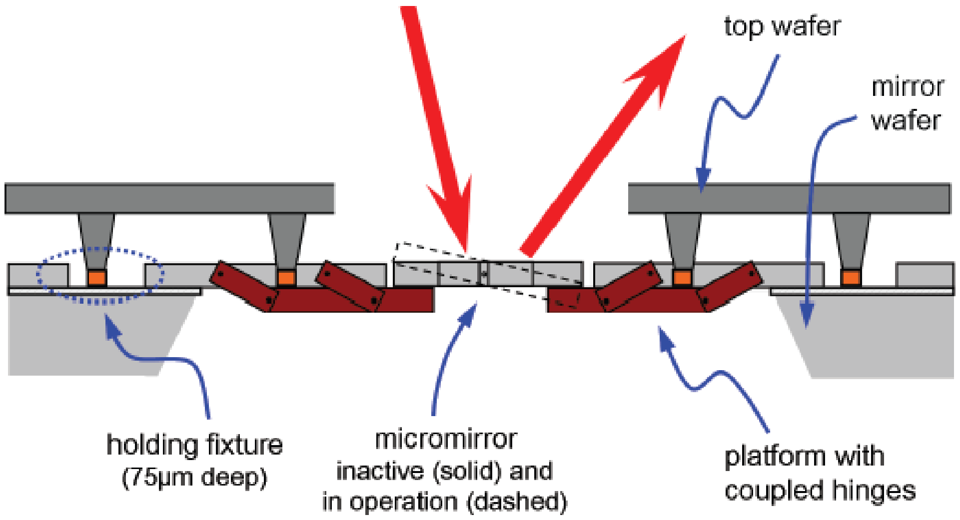

Figure 1.16 Schematic illustration of the functional principle. During the wafer bonding the stamps of the top wafer are pressing on the deflection pads of the mirror wafer. Via coupled hinges the downward motion of the pads is transferred into a vertical deflection of the comb-drive counter electrode [51].

In 2011, Kallweit et.al [51] presented a new developed quasistatic-resonant micromirror capable of performing fast resonant sinusoidal as well as slow linear static scanning. In this design, the in-plane fabricated comb-drive actuators undergo a vertical out-of-plane deflection when being combined with an applicable top wafer as shown in Fig. 1.16. During the wafer assembly the down pressing stamps of the top wafer displace some platforms, which are connected via coupled hinges with one part of the opposing actuation electrodes and make them move out of plane in well defined manner. Although the performance of this scanner is not reported, it is a promising step to achieve electrostatically actuated 2D scanner with linear slow axis.

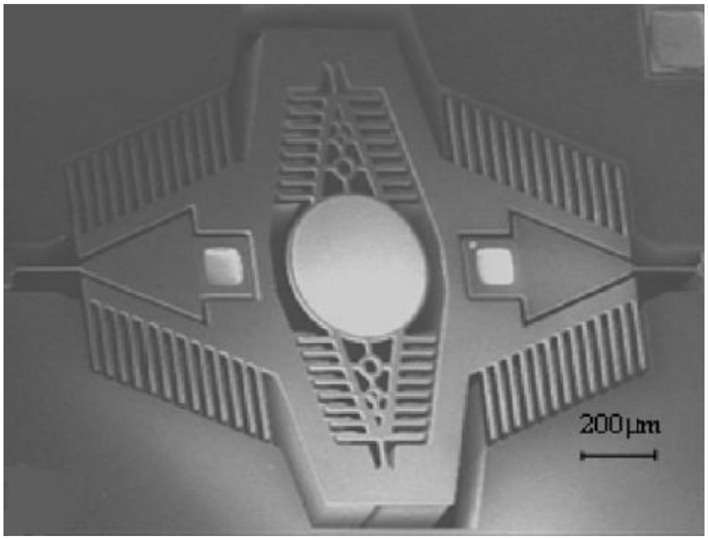

Figure 1.17 SEM of the fabricated microscanner [52].

Moreover, Chu et.al [52] reported a 2-D comb-drive scanner (Fig. 1.17) that operates with double resonant principle. The resonant frequencies of the inner mirror and the gimbal frame are 40 kHz and 162 Hz, respectively. The resonant frequency ratio is 247. The optical scanning angles for the inner mirror and the gimbal frame are 11.5 deg. and 14 deg. at the operation voltages of 12 and 10V in 1 Pa vacuum, respectively.

1.5.3 Piezoelectric Actuated Scanners

As mentioned earlier, designing a non-resonant scanner with piezoelectric actuation is a challenging task. Although there are piezoelectric actuated 2D scanners that have resonant operation for both axes [53-55], there are few successful scanners that have both resonant and non-resonant scanning capabilities with piezoelectric actuation. As explained in Chapter 2, preferred architecture for MEMS scanner based laser display is constituted with both a high frequency resonant horizontal scan and a non-resonant linear ramp scan. Thus, 2D scanners without a non-resonant scan capability are not interesting for high-resolution displays.

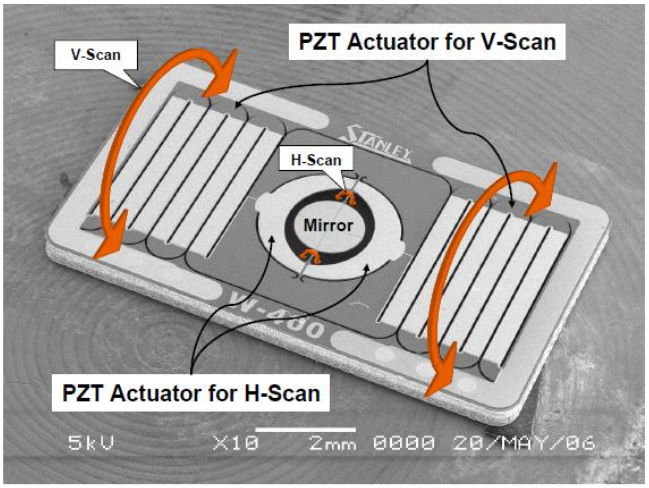

Figure 1.18 SEM micrograph of the developed 2D scanner. It consists of meandering PZT suspensions for the vertical scan (V-Scan) and fast axis actuators for the horizontal scan (H-Scan) [45].

In 2006, Tani et.al presented a 2D scanner (Fig. 1.18) that has a combination of fast resonant mode and a slow non-resonant mode [45]. In this work, 2D scan is demonstrated with a resonant operation at 11.2 kHz for the fast horizontal axis with ±39° optical scan angle and quasi-static operation at 60 Hz of the slow vertical axis with ±29° optical scan angle operated at 40 V_{pp}. Although resonant frequency of this scanner is lower for high-resolution displays, it is the first successful demonstration of piezoelectric actuated 2D scanner with both fast and slow mode operation in literature.

1.6 Contributions of the Thesis

This thesis reports design, simulation, fabrication and characterization results of two different scanners: first one is an electrostatically actuated non-resonant MEMS stage designed to operate at 60Hz, and the second one is a piezoelectric actuated resonant MEMS mirror designed to operate at high-frequencies. Specifications for both scanners are derived from mobile display applications.

In Chapter 2, a novel rotary MEMS stage is discussed. In-plane motion of a MEMS device restricts the suspension design to one using bending flexures. Such flexures have one end fixed to a substrate and the other end attached to the moving body and the clamped–guided boundary condition typically results in cubic spring stiffening. In this work, a new spring design is developed to enable the rotary MEMS stage to rotate up to 7 deg. with 98% linear in-plane motion. Its linearity figure is superior to its counterparts in the current literature. With the integration of a mirror, this stage can provide a linear ramp scan for the slow axis of a two-mirror display engine.

In Chapter 3, a high frequency thin film PZT actuated MEMS scanner is presented as the fast axis component of the two-mirror display engine. Although PZT actuators provide several advantages over electrostatic and electromagnetic actuators, they generally generate small displacement. In this work, PZT actuators are used on the outer frame of the mechanically coupled structure so that their small displacement amplified ten times into inner frame where mirror stands. This way, optical rotation angle of 38.5 deg. is achieved with 1.4 mm mirror which operates with 24 V at 40 kHz resonance. Considering its rotation angle capability at a high frequency operation, it exceeds the performance specifications cited in the current literature, and becomes a significant step towards achieving full HD resolution with mobile laser projectors.

Relevant Publication:

Pending Patents

1. Wyatt Davis, Hakan Urey, Dean Brown, **Utku Baran**, Jason Tauscher, Sven Holmstrom, "Rotating MEMS Scanner", US Patent Pending, filed in July 2011 (Licensed to Microvision Inc., USA)

2. Wyatt Davis, **Utku Baran**, Dean Brown, Hakan Urey, "Resonant MEMS Scanner", US Patent Pending, filed in January 2012 (Licensed to Microvision Inc., USA)

Journal Publications

1. **U. Baran**, W. Davis, S. Holmstrom, D. Brown, J. Sharma, S. K. Gokce, H. Urey, "Linear-Stiffness Rotary MEMS Stage", IEEE JMEMS, Vol. 21, No. 3, pp. 514-516, (2012)

2. **U. Baran**, Dean Brown, S. Holmstrom, D. Balma, W. Davis, P. Muralt, H. Urey, "Resonant PZT MEMS Scanner for High Resolution Displays", IEEE JMEMS (accepted, in press)

Conference Proceedings

3. **U. Baran**, W. Davis, S. Holmstrom, D. Brown, J. Sharma, S. K. Gokce, H. Urey, "MEMS rotary stage with linear stiffness", IEEE Optical MEMS and Nanophotonics (OMN), 2011 International Conference, vol., no., pp.37-38, 8-11 Aug. 2011

4. **U. Baran**, D. Brown, S. Holmstrom, D. Balma, W. Davis, P. Muralt, H. Urey "High Frequency PZT Torsional MEMS Scanner for Displays", IEEE MEMS 2012, Paris, France, Jan. 29 – Feb. 2, 2012

2 COMB-ACTUATED LINEAR STIFFNESS ROTARY MEMS SCANNER

2.1 Introduction

For a projector engine the scanning motion needed is obtained either by one bidirectional scanner or by a separate high frequency scanner for the horizontal axis and a low frequency scanner for the vertical axis (Fig. 2.1). The vertical axis is typically driven quasi-statically with a saw-tooth signal to achieve a linear 2D raster. A less researched option for the vertical axis scan is the in-plane rotary scanner with a vertically mounted mirror. Large in-plane rotations of a suspended body are desirable for several applications, including optical scanning [42, 43], angular rate sensing [56, 57], tunable lasers [58], optical switchers [59], optical attenuators [60], and compasses [61]. A challenge for these types of devices for display application is to make them respond linearly to the actuation amplitude while achieving a compact form-factor.

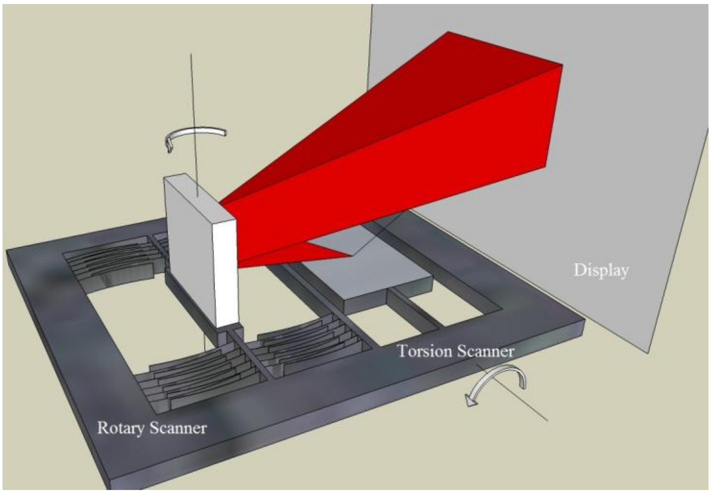

Figure 2.1 Schematic of a flying spot laser display engine with two mirrors.

Electrostatic (ES) comb-drive scanners are relatively simple to fabricate and can be compact, with the tradeoff of requiring very high voltage. However, typical out-of-plane comb scanners for laser beam scanning applications are only suitable for resonant actuation and do not respond to DC [37]. This can be addressed by making off-set comb fingers [38, 39] or by using electrodes on a separate wafer [40, 41]. However, scan angles are limited and linear scan motion is difficult to achieve as the electrostatic force is geometrically nonlinear. As an alternative, in-plane rotation using curved comb fingers can also be used as resonant scanning platform for laser scanning applications [42], but in-plane scanners are affected by the nonlinear spring stiffening of suspension beams used in bending mode. Nonlinear stiffening of the suspension members can limit the quasi-static rotation amplitude that can be achieved with the available forcing amplitude, and so, it is desirable for the suspension members to provide a constant linear stiffness. For micro-electro-mechanical systems (MEMS) devices, micro-machined torsion beams are effective at providing linear stiffness for large out of plane rotations, but these are not very practical to implement for devices intended to operate in plane. In-plane motion of a MEMS device restricts the suspension design to one using bending flexures. Such flexures will have one end fixed to a substrate and the other end attached to the moving body. The clamped–guided boundary condition will typically result in cubic spring stiffening [62]. This nonlinearity will limit the achievable quasi-static displacement for the forcing amplitude available from the actuator, as demonstrated in [42] and [63], and will produce jump discontinuities and hysteresis in the frequency response (i.e., the classic response characteristics of a Duffing oscillator) [64]. Since the nonlinear stiffening arises from axial tension developing in the suspension beams, previous approaches to managing the nonlinear stiffening for in-plane rotational suspensions have involved introducing extra axial compliance, for example, by flexure folding or meandering, as in [57] and [65], or making the connection to the fixed substrate using a “tee” bending member [42]. These approaches will reduce but not eliminate the cubic stiffening.

This chapter demonstrates a different approach that seeks to exploit a special case of clamped–guided beams that have identically zero cubic stiffening without folding or attempts to form compliant boundary conditions. Accordingly, in this thesis, a novel spring design is introduced to achieve linear in-plane rotary stiffness. A MEMS rotary stage featuring a bending flexure suspension with linear stiffness has been designed, fabricated, and characterized. The stiffness linearity is demonstrated by the insignificant shift in the resonance frequency of the rotational mode with increased angle and by the linear relation between rotational angle and voltage up to $\pm 7^\circ$ motion at resonance. Pull-in behavior is observed at relatively low voltages, which will be corrected in future devices by improved designs and use of wider comb fingers. The device is intended to be actuated quasi-statically at 60 Hz to enable its use as the slow-axis scanner for laser projection systems. The spring structure could also be implemented for precise control of valves in microfluidic applications or mounting various micro-optical, mechanical, or nanophotonic structures on the compact rotary stage and forming an array of such devices for beam steering and optical switching applications.

The theoretical motivation developed in Section II. The device design and fabrication process and a finite element model are described in Section III-V, and the device is characterized and the results are reported in Section VI. Finally, Section VII mentions about future work.

2.2 Theory

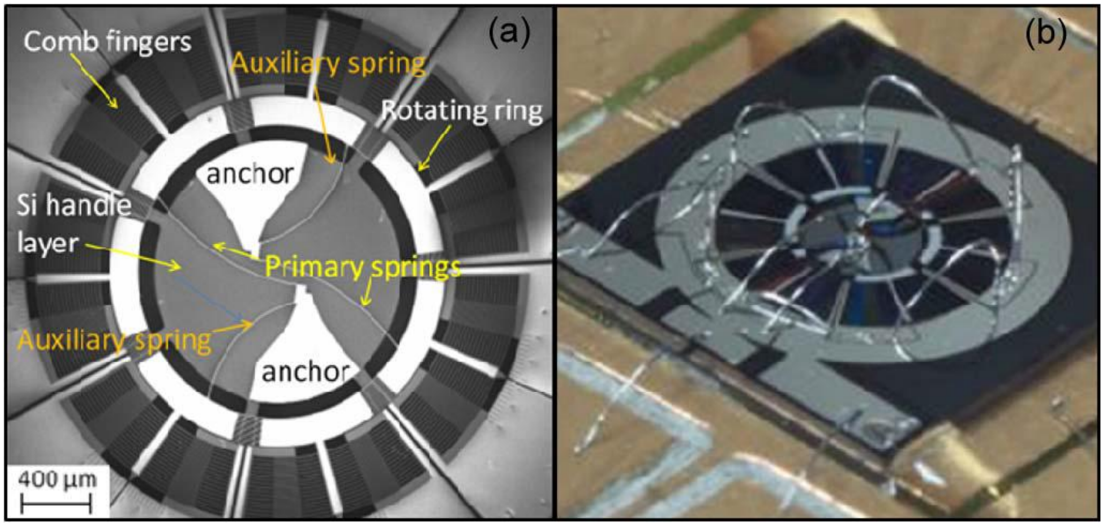

Figure 2.2 (a) SE micrograph of the rotary stage. (b) Photograph of a wire-bonded device.

The design goal for the rotating ring suspension is to achieve linear stiffness for large in-plane rotations. Clamped–guided beams will typically exhibit nonlinear stiffening already when the maximum displacement is only a fraction of the beam’s width. Exact formulas for the coefficients of cubic stiffening for three cases of clamped–guided boundary conditions were derived in [62] and [66]. It was noted in [66] that the case of a rotating ring with an interior suspension has a vanishing of the cubic stiffness coefficient for two particular ratios of the radius to the length. The exact coefficient of cubic stiffening k_3 for this case is

$$k_3 = \frac{2EA}{225L^3}\left(L^2 - 9LR + 9R^2\right)^2 \tag{2.1}$$

where E is the elastic modulus, A is the cross-sectional area of the beam, R is the inner radius of the suspended ring, and L is the length. This coefficient is zero for R/L = 0.87 and R/L = 0.13. However, both of these special cases require suspension beams to cross each other, which makes it impossible to form them out of a single structural layer [66].

Fig. 2.2a shows a scanning electron (SE) micrograph of a micro-fabricated rotating ring with a rotary comb drive actuator and a suspension that approximates one of these special cases. The anchors for two "primary" beams were positioned near the ideal location R/L = 0.87 but with an offset that permitted them to be formed in the same structural layer and to deform without interfering with each other. This offset results in a nonzero k_3; however, a curvature was introduced and fine tuned using finite-element analysis until the desired linearity was recovered.

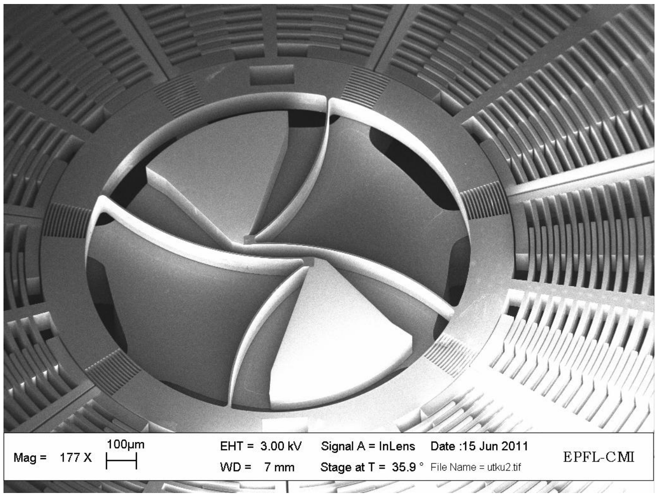

Figure 2.3 SEM picture that shows the side view of the device.

Furthermore, two additional "auxiliary" suspension beams sharing the anchors were added to suppress the tendency of the ring to undergo out-of-plane torsion. The dimensions and the curvature of these auxiliary beams were also designed for the stiffness to remain linear over the desired range of the in-plane rotation. The novel suspension with approximately linear stiffness, which approximates the ideal special case *R/L* = 0.87 for straight beams, is shown in Fig. 2.2a. A side view is shown in Fig. 2.3.

2.3 Device Design

100-μm-thick and 75-μm-thick MEMS rotary devices are 3 mm in diameter. Two anchors are placed inside a circular stage as illustrated in Fig. 2.4a. Each anchor is connected to the ring through two (5-6)-μm-wide and flexures. To lower peak stresses, the corners of the flexures' connection points are rounded. Moreover, to each side of seven comb arms protruding from the ring, concentric comb actuators are attached. These are interdigitated with static comb fingers. Angular electrostatic comb actuators are bound by arms to the ring, as shown in Fig. 2.4, to enable the rotational motion.

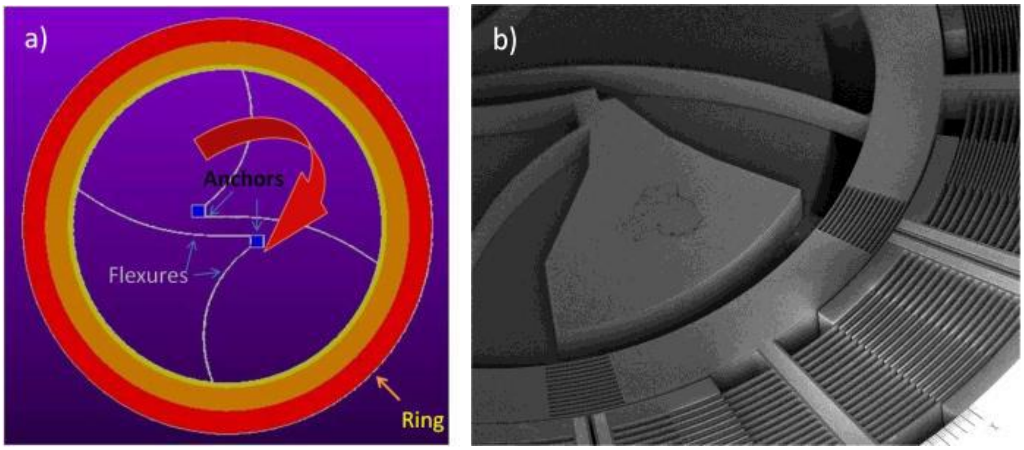

Figure 2.4 (a) Sketch of the stage. (b) SEM Picture of the stage showing flexures and comb actuators.

The anchors’ locations are arranged to an approximate optimum design point which is difficult to realize in practice as explained in [66]. Although the device is designed to be able to carry 4.76 mm × 2.8 mm × 0.15 mm mirror, this thesis is focused on the development of the scanning platform without mirror by optimizing the locations of the anchors and shapes of the flexures to obtain high linearity in rotation and overcome the strong tendency of clamped-guided beams to exhibit nonlinear stiffening.

2.3.1 Required Voltage Calculation

The required DC voltage $V_{required}$ to quasi-statically rotate the stage at an angle θ can be calculated from below formula [67]

$$V_{required} = \sqrt{\frac{2k_m \times \theta}{\partial C / \partial \theta}} \tag{2.2}$$

where k_m is the stiffness and C is the total capacitance between the comb actuators which is calculated from

$$C = 2\varepsilon_0 \times t \times \frac{R_{average} \times N_{finger} \times N_{arms} \times \theta}{g} \tag{2.3}$$

where ε_0 is the dielectric constant, t is the thickness, $R_{average}$ is the average distance of the comb fingers to the center, N_{finger} is the number of fingers on each arm, N_{arms} is the number of arms, and g is the gap between comb fingers.

2.4 Fabrication

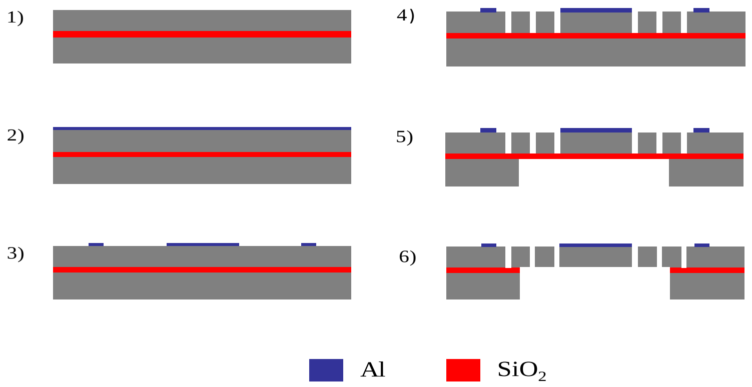

Figure 2.5 Fabrication flow of Rotary Stage.

The microfabrication is performed with a three-mask process using silicon-on-insulator wafers with a highly doped 100-µm-thick and 75-µm-thick device layers as starting material (Fig 2.5(1)). The first fabrication step is to sputter and pattern 400 nm of Al to form the wire-bond electrodes as well as the measurement gauge (Fig 2.5(2-3)). The front-side device structures and the back-side opening are then defined through photolithography and etched with deep reactive ion etch (DRIE) (Fig 2.5(4-5)). After back-side DRIE to remove handle layer silicon from beneath the actuator, the devices are released by etch of the buried oxide in HF vapor (Fig 2.5(6)). Since part of the actuator still sits on top of handle layer silicon, a few micrometers of side etch is needed to fully release the structure. Finally, 4.76 mm × 2.8 mm × 0.15 mm mirror is placed on the rotary stage manually using UV cured epoxy.

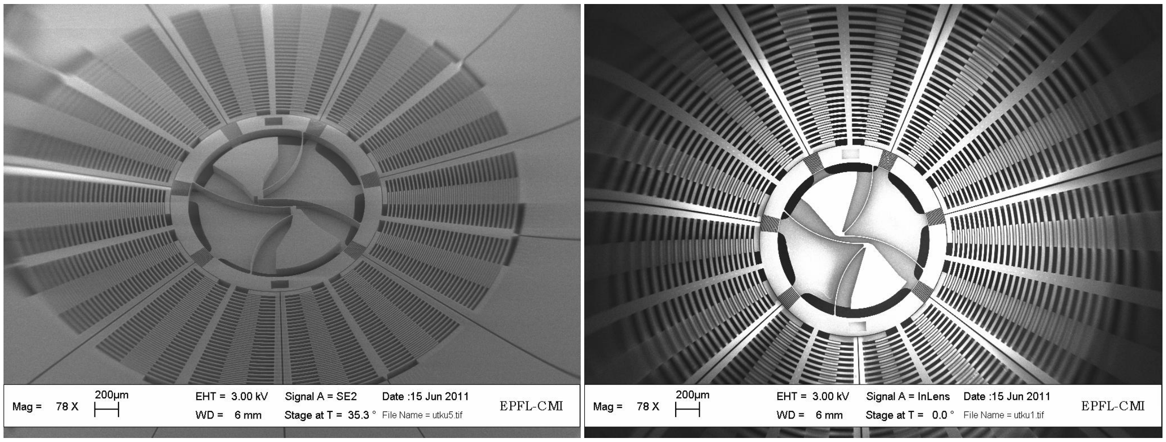

Figure 2.6 SEM images of the fabricated devices.

2.5 Finite-Element Modeling

2.5.1 Modal Analysis

The device is intended to be actuated at 60 Hz non-resonant frequency to enable its use as the slow-axis scanner for laser projection systems. Distortions that may come from the higher modes drastically harm the purity of the rotational motion. Hence, there are two major aspects while engineering the vibration modes: The in-plane rotation mode should be placed at the lowest resonance frequency and the other modes should be well separated from the in-plane rotation mode to avoid unwanted coupling. To achieve this, finite-element analysis (FEA) software, ANSYS, was used to predict the modes of the structure. It is found that when a large mirror is mounted on the stage, mode separation gets worse and torsion modes come closer to the rotary mode due to the relatively large inertia of the mirror.

Modes	Frequency (Hz) for Stage Only	Frequency (Hz) for Stage with Mirror
1st	**581** (Rotary)	**270** (Rotary)
2nd	**2871** (torsion wrt. 45 deg. axis)	**400** (torsion wrt. 45 deg. axis)
3rd	**4030** (vertical in plane sliding)	**579** (torsion wrt. other 45 deg. axis)
4th	**4050** (torsion wrt. other 45 deg. axis)	**2628** (vertical in plane sliding)
5th	**5501** (horizontal in plane sliding)	**3774** (horizontal in plane sliding)

Table 2.1 Modal analysis result shows the frequencies of first five resonant modes of 100-µm-thick device.

Modes	Frequency (Hz) for Stage Only	Frequency (Hz) for Stage with Mirror
1st	**487** (Rotary)	**254** (Rotary)
2nd	**1587** (torsion wrt. 45 deg. axis)	**314** (torsion wrt. 45 deg. axis)
3rd	**2413** (vertical in plane sliding)	**461** (torsion wrt. other 45 deg. axis)
4th	**3095** (torsion wrt. other 45 deg. axis)	**2518** (vertical in plane sliding)
5th	**4512** (horizontal in plane sliding)	**3610** (horizontal in plane sliding)

Table 2.2 Modal analysis result shows the frequencies of first five resonant modes of 75-µm-thick device.

Device thickness’ effect on mode separation is investigated to find the optimum thickness to get better mode separation. It is found that thicker the device, better the mode separation, worse the voltage requirement. 75-µm-thick and 100-µm-thick devices are picked as best candidates to fabricate. Using FEA, the rotary mode for stage is estimated as 581 Hz for 100-µm-thick device. All higher modes are above 2500 Hz, well separated from the principal mode (Tab. 2.1). Result of modal analysis for 75-µm-thick device is also shown in Tab. 2.2.

2.5.2 Static Analysis

Large-displacement static analysis is performed to investigate the linearity of the spring. In order to speed up the iteration time, ANSYS macro written by Dean Brown, Microvision Inc., is used. With the help of this macro, rotational stiffness of the stage and the deviation from the linear case is calculated and plotted in the same picture with other parameters (Fig. 2.7).

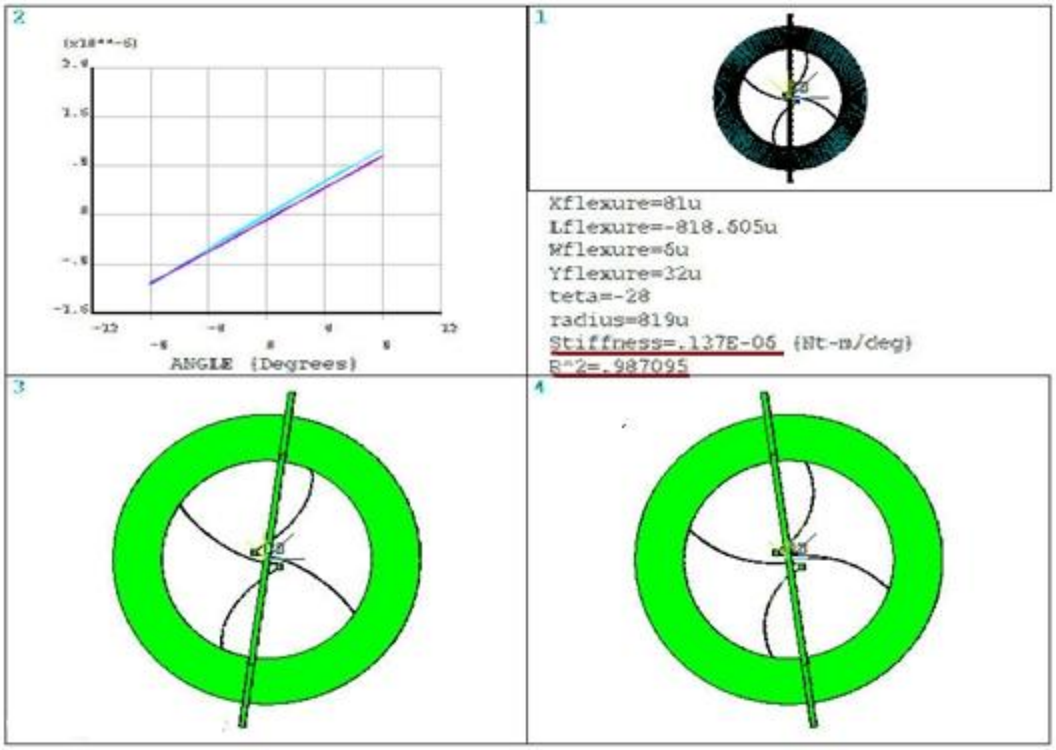

```
Xflexure=81u
Lflexure=-818.605u
Wflexure=6u
Yflexure=32u
teta=-28
radius=819u
Stiffness=.137E-06 (Nt-m/deg)
R^2=.987095
```

Figure 2.7 Macro plot shows the stiffness and the deviation from linearity as a result of static analysis.

The simulated stiffness deviation from linearity was found only 1.5% for up to +/-10 deg. mechanical rotation (corresponding to 40 deg. total optical scan angle) which is better than its counterparts in the literature [42, 58, 65], and it fits well with the experimental results.

2.6 Mechanical Characterization Results

2.6.1 Drive Characteristics

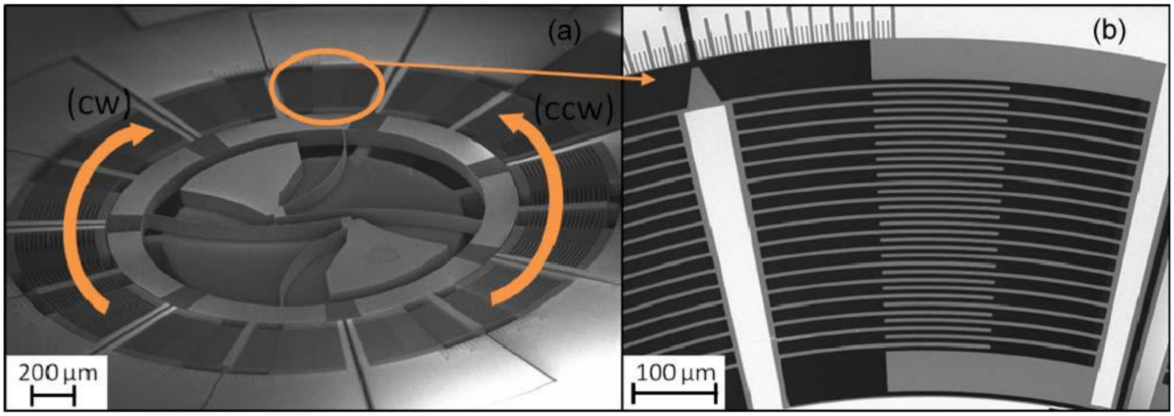

Figure 2.8 (a) SE micrograph of the entire device with the arrows showing the cw and ccw directions, respectively. (b) Close-up SE micrograph of one set of comb fingers pulling the platform in the cw direction. The gauge used to measure the rotation can be seen at the top.

The device is divided into three isolated potentials. The rotational platform is electrically connected through wire bonds to the anchors. The static comb-fingers driving the platform clockwise (cw) are all connected through the device layer silicon. On the other hand, due to the geometric necessity the static comb-fingers pulling the platform counterclockwise (ccw) are electrically isolated by isolation trenches and connected with each other through wire bonds (Fig. 2.8a).

In order to have a linear in-plane comb actuation, differential driving voltages (A, B) are used for each direction as below

$$A = DC + |AC|\sin(\omega), B = DC - |AC|\sin(\omega) \tag{2.4}$$

Since it is not possible to acquire a scan line without mounting the mirror on the stage, imprinted scale is used to measure the rotation angle (Fig. 2.8b). The scale has notches at every quarter degree, limiting the measurement resolution accordingly.

2.6.2 Experimental Results

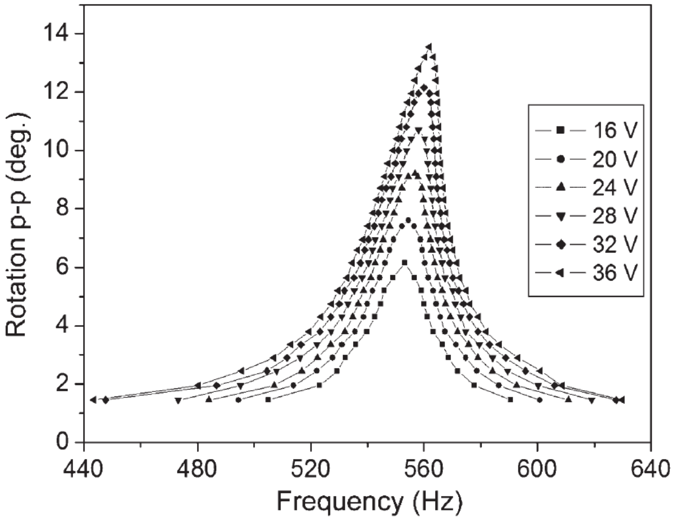

Figure 2.9 AC voltage amplitude as a function of frequency at several levels. Up to a peak-to-peak rotation of 10 deg., the frequency shift is less than 1%.

After fabrication, it was observed that the side etch during DRIE had been larger than expected. Related with this, the comb-fingers and flexures were 1-2 μm thinner than designed for. Moreover, asymmetric motion is observed during experiments, which is believed to be caused by the undesired frequency distance between 2nd and 3rd modes. Due to these problems, required excitation voltages went up and the pull-in voltage threshold went down to 40V.

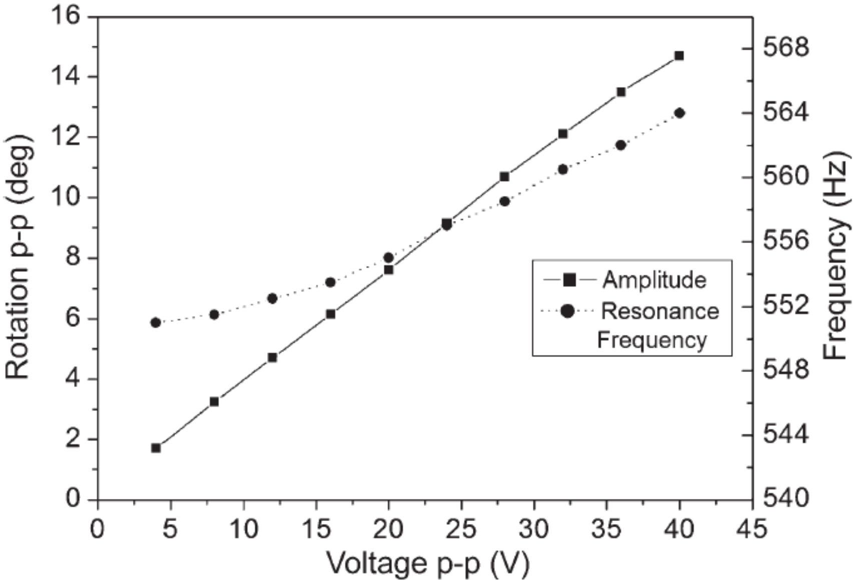

Figure 2.10 Resonant deflection and resonant frequency as a function of excitation voltage. The frequency is adjusted at each voltage level to maximize the deflection. The rotation angle is measured via the imprinted scale.

The present device's pull-in voltage of 40 V allowed for only 1 deg. one-sided rotation for quasi-static actuation. Due to this limited deflection, the linearity of the stiffness could not be shown by non-resonant quasistatic actuation. In order to assess the rotational linearity, a collection of frequency response curves with various amplitude levels are taken at ambient pressure, as shown in Fig. 2.9. The resonant frequency is around 555 Hz, which is close to the FEM prediction. The peak value for each voltage was measured using a gauge and a scale imprinted on the device frame, as shown in Fig. 2.8b. Although there is little evidence of nonlinear spring stiffening with a slight resonance frequency shift of only about 1% up to 15 deg. peak-to-peak rotation, these results clearly demonstrate a linear spring behavior well above that of conventional clamped–guided beams. There are no jump discontinuities in the frequency response, in contrast to other devices in the literature that use bending beams for a rotary suspension [42].

Fig. 2.10 shows the deflection at resonance as a function of voltage and the little change in resonance frequency with increased amplitude. The data are again taken by using the imprinted scale. In this experiment, the device is actuated with a differential drive voltage with an offset of 20 V. The resulting linear regression coefficient is larger than 0.99.

The device rotates more than ±7 deg. when actuated with 40 V at ambient pressure. These tests safely prove that the spring design keeps linear stiffness for large rotation angles.

2.7 Summary and Discussion

A MEMS rotary stage featuring a bending flexure suspension with linear stiffness has been designed, fabricated, and characterized. The stiffness linearity is demonstrated by the insignificant shift in the resonance frequency of the rotational mode with increased angle and by the linear relation between rotational angle and voltage up to ±7 deg. motion at resonance. Pull-in behavior is observed at relatively low voltages, which will be corrected in future devices by improved designs and use of wider comb fingers.

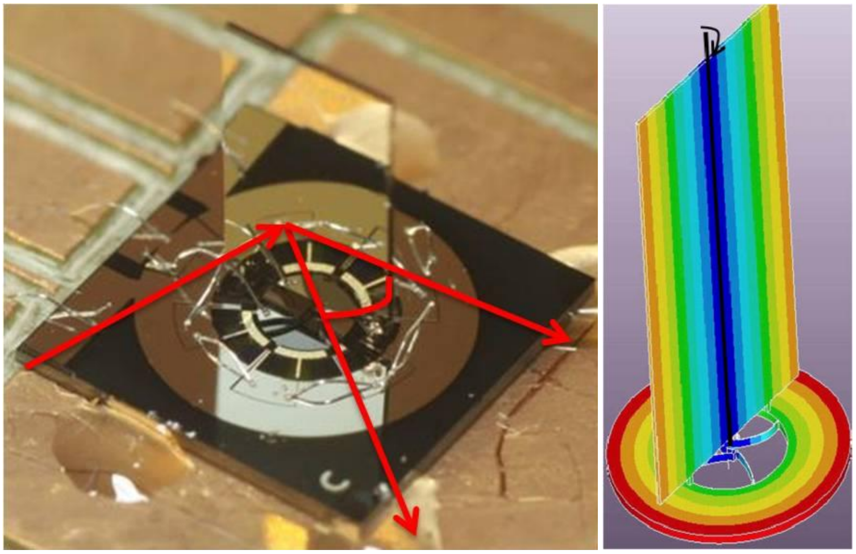

Figure 2.11 (a) Demonstration of the scanner with a mounted mirror on the rotary stage. (b) Concept sketch with a mounted mirror.

A future application of this rotary stage is as an actuator for a quasi-static scanning mirror. Successfully mounted mirror on a broken stage, and a finite-element model of the envisioned device is shown in Fig. 2.10. The device is intended to be actuated quasi-statically at 60 Hz to enable its use as the slow-axis scanner for laser projection systems. Future work will focus on mounting a perpendicular mirror on top of a working stage. The spring structure could also be implemented for precise control of valves in microfluidic applications or mounting various micro-optical, mechanical, or nanophotonic structures on the compact rotary stage and forming an array of such devices for beam steering and optical switching applications.

3 PIEZOELECTRIC ACTUATED RESONANT MEMS SCANNER

3.1 Introduction

Commercial interest for mobile pico projectors has increased rapidly in recent years, driving the interest for high performance scanners [12]. Such scanners for laser display applications typically require actuators that can provide a large scan angle with a large mirror at high frequency and a low driving voltage. The requirements for horizontal MEMS scanners for use in a laser scanning based high-resolution display were reported in [11]. Single-crystal-silicon (SCS) is usually utilized at resonant mode operation to satisfy the requirements for frequency and scan angle.

The majority of the best performing resonant scanners in the literature are either electromagnetically (EM) or electrostatically (ES) actuated. EM scanners require the placement of bulky off-chip magnets close to the scanning device leading to increased package size. On the other hand, ES comb-drive scanners are fairly simple to fabricate and can be compact, but they require high drive voltages. In addition, several scanning MEMS mirrors actuated by applying voltage to stack lead zirconate titanate (PZT) layers have been reported [68]. In a few cases this is done with an asymmetric design excited by an external PZT stack attached to the chip [69, 70]. However, it is difficult to fabricate such devices monolithically via the silicon wafer process and stack PZT actuators consume space, as is the case with EM actuators. Hence, when key features for scanning MEMS mirrors, such as achieving large deflection with a low voltage in a small package are considered, exploring new actuation mechanisms remains an important and challenging task.

As stated earlier, scanners actuated by piezoelectric thin films use much lower voltages than ES scanner and share their smaller form factor advantage. Moreover, piezoelectric actuators can measure deflection from the piezoelectric voltage of the separated electrode [18] or the piezoelectric current charge [19]. Thus, they can be used as angle sensors for closed-loop control of micro scanners without any additional process or material.

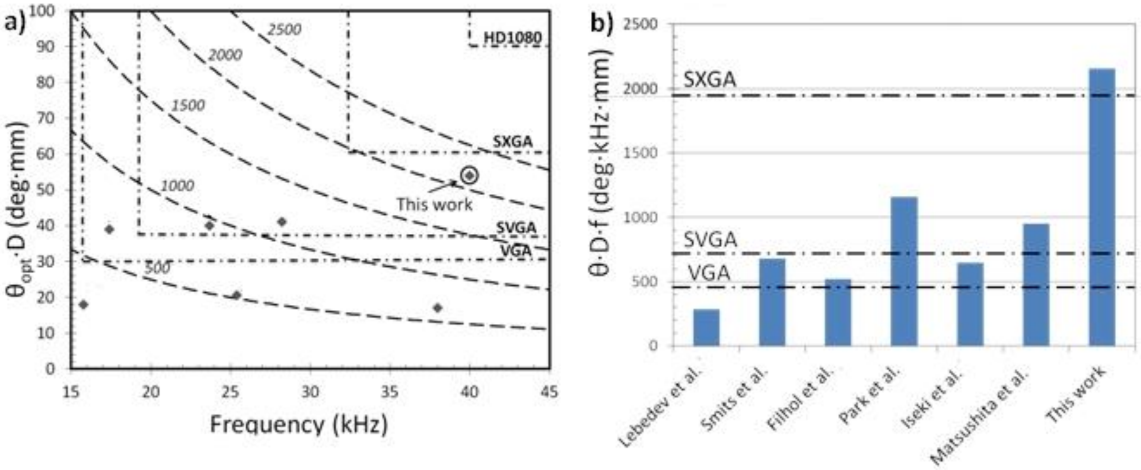

Figure 3.1 (a) Performance comparison of piezoelectric thin film actuated microscanners based on the literature [29-31, 33, 71-73]. The dashed arcs indicate selected levels of $\theta_{OPT}\times D\times f$ products in deg×mm×kHz for better comparison of scanners between different working frequencies. The dash-dotted squares show requirements for different display formats assuming 60 Hz refresh rate and bidirectional scanning. (b) Performance comparison of piezoelectric thin film scanners according to $\theta_{\mathrm{OPT}}\cdot D\cdot f$ metric. The dash-dotted lines show the borders of the various display resolutions.

Although thin film PZT actuation is a promising candidate to meet the requirements of both high power density and size for mobile laser projectors, mechanical design challenges still remains to be solved. For high frequency resonant PZT scanners, damping losses at high frequencies and limited deflection of PZT beams with large stiffness are the two main obstacles to overcome. In earlier research, the small deflection of the PZT film lead to designs that utilize long actuation levers in order to achieve high optical scan angles. However, this approach tends to fail for high frequency devices where the mechanical instability and high dynamic deformation requirements are not trivial to satisfy.

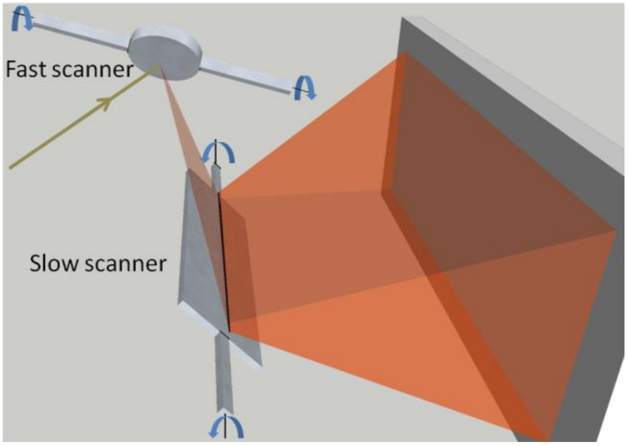

Figure 3.2 The scanner presented in this paper could perform the horizontal fast scanning in a high resolution laser projection system.

This thesis introduces a novel actuation scheme that combines PZT thin-film actuation with the principle of mechanical amplification, previously used for EM-actuated and ES-actuated scanners [9, 26], to achieve high performance PZT actuated resonant MEMS scanners. Fig. 3.1 compares reported PZT thin film actuated scanner performances according to a combined figure of merit $\theta_{OPT} \cdot D \cdot f$ which indicates the possible rate of pixels per seconds. θ_{OPT} is the optical scan angle, D is the mirror width along the scan direction, and f is the scan frequency. According to these metrics, the present scanner is the best performing high frequency resonant MEMS scanner in literature. It could provide the fast horizontal scan for a two mirror laser projection system, as shown in Fig. 3.2.

This scanner is a significant step towards achieving full HD resolution (1920 x 1080 pixels) in mobile laser projectors. Reported piezo scanner requires no bulky components and consumes <30mW power at maximum deflection, thus provides significant power and size advantages compared to reported electromagnetic and electrostatic scanners. Interferometry measurements show that the dynamic deformation is at acceptable levels for a large fraction of the mirror and can be improved further for diffraction limited performance at full resolution. A design variation with a segmented electrode pair illustrated that reliable angle sensing can be achieved with PZT for closed-loop control of the scanner.

The device design and fabrication process are developed in Section II. The finite element model is described in Section III, and the device is characterized and the results are reported in Section IV. Finally, Section V provides summary.

3.2 Design and Fabrication

3.2.1 Device Design

The presented scanner consists of two cascaded frames. The outer frame is the actuator and is referred to in Fig. 3.3 as PZT A-B. When a voltage is applied between the bottom and top electrodes, the outer frame deforms due to the longitudinal expansion in the PZT layer. This motion is directly coupled into the mirror on the inner frame.

The inner frame holds the scanning mirror and is carefully designed to limit the dynamic deformation of the mirror. The outer frame is anchored to the substrate, and the inner frame is attached to the outer frame via torsional flexures. PZT thin-film actuators are placed on each side of the outer frame as shown in Fig. 3.3. Any cascaded two-frame mechanical structure will have two separate rotation modes: the two frames rotate in-phase or they rotate out-of-phase. The present device is designed to rotate the large mirror at the out-of-phase-resonance with a large angular amplification.

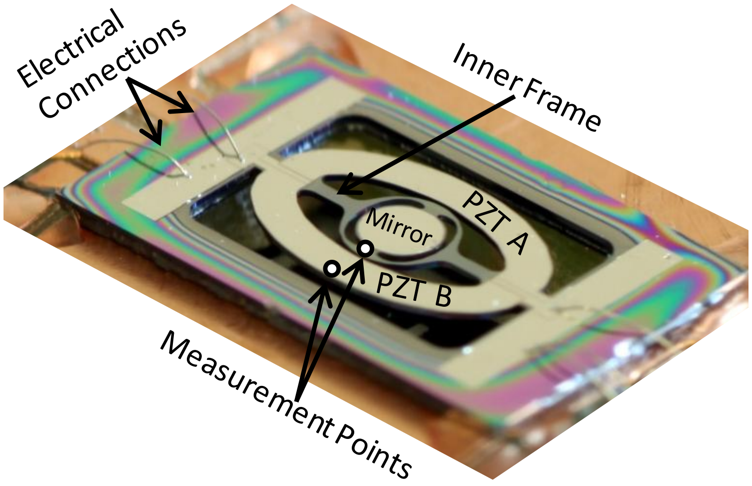

Figure 3.3 Photograph of a scanner wirebonded to a custom made PCB. The major structural components of the device are pointed out as well as the two points used for amplitude measurements. PZT A and B are the complementary drive electrodes that together make up the outer frame.

There are two main advantages of the cascaded PZT operated in out-of-phase arrangement compared to a mechanism without an outer frame (i.e. a direct drive, where the PZT actuators are attached directly to the mirror). Firstly, larger scan angles can be achieved by keeping the scan mirror and inner flexures small and without additional stress inducing layers. Secondly, the limited deflection of the PZT thin-film actuator can be amplified to achieve large mirror rotation at resonance. The problem with the previously reported PZT actuators with long lever arms is achieving good mode separation without crosstalk and poor shock and vibration survivability due to long flexures.

The device has a 3.75 mm x 6.15 mm die size and is 125 μm thick. The entire structure is anchored to the substrate with a main suspension system consisting of two 220 μm long and 520 μm wide flexures. The inner frame, in turn, is attached to the outer frame by a pair of 480 μm long and 270 μm wide flexures. To lower the peak stress, the corners of the connection points of the flexures are rounded. The scanner employs a 1 mm × 1.4 mm oval mirror in the inner frame. Two main strategies are employed in order to diminish dynamic deformation of the mirror. A 175 μm thick cross shape backside reinforcement rim is used to increase mirror stiffness and, secondly, the mirror is mechanically isolated from the rotational flexure with an isolation frame, as illustrated in Fig. 3.3.

3.2.2 Fabrication

The microfabrication is performed with a six-mask process using silicon-on-insulator (SOI) wafers having a 125-μm-thick device layer as illustrated in Fig 3.4. The first fabrication step is to thermally grow 2 um thick SiO_2 layer on both sides of the wafer. The bottom electrode was deposited on the oxidized wafers with a *Balzers BAS 450* multi-target sputtering system, at 300°C. It consists of a $Pt/TiO_2/Ti$ stack with thicknesses of 100/50/3/ nm, respectively. The Ti was used as an adhesion layer, the TiO_2 as a barrier layer to prevent the diffusion of titanium to the top surface of the platinum, or also to prevent reaction of lead with SiO_2. The textured Pt(111) film serves as electrode and as growth substrate for obtaining a highly (100)c-textured $PbTiO_3$ (PTO) film (20 nm thick) used as template for the growth of the subsequent 2 μm thick PZT(100) film [74]. PTO and PZT were deposited by a sol-gel technique based on an improved 2-methoxyethanol route.

The PTO film was the result of one spin, one pyrolysis step and one rapid thermal annealing step (60 s at 650 °C). The 2 μm thick PZT film was deposited with 8 annealing steps (650 °C), each consisting of 4 solution spinning (4000 rpm for 40 s) and pyrolysis steps (350 °C for 60 seconds). The 4 solutions had lead excess concentrations of 10% for the first three, and 30% for the last layer, to compensate for lead evaporation during annealing. The temperature ramp during annealing was optimized in order to achieve the desired perosvkite phase with (100) orientation. The average Ti to Zr ratio was chosen to be the one of the morphotropic phase boundary, i.e. $Pb(Zr_{53}Ti_{47})O_3$, in order to maximize the piezoelectric properties. The solutions could still be improved concerning the Ti/Zr concentration homogeneity as described in reference [75]. As a last deposition step, a 100 nm thick Pt top electrode layer was evaporated and patterned using a lift-off process on the PZT layer (Mask 1).

Next, the backside oxide is patterned with photolithography and dry etch (Mask 2). This patterning is later used to create the backside mirror reinforcement. In order to protect the reinforcement areas beneath the mirror during backside silicon etch, backside SiO_2 layer is patterned so that the 2-μm-thick SiO_2 protective layer is left on the reinforcement areas. The desired geometry of the PZT was defined by patterning with 8 μm thick AZ 9260 photoresist, and wet etching (Mask 3). The 2 μm PZT layer is wet etched in a chemical solution consisting of 30% of DI water, 70% of chloride acid (diluted at 30%) and a few droplets of hydrofluoric acid (diluted at 40%). The etch rate was about 1 μm/min. By contrast, after patterning the PZT film, the bottom electrode is etched in chlorine chemistry using a *STS Multiplex ICP* dry etcher after being defined through photolithography (Mask 4).

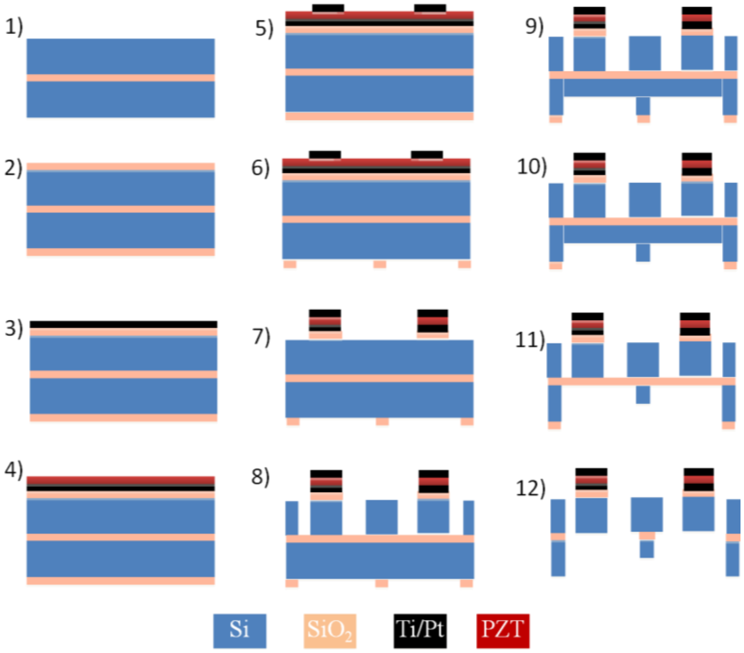

Figure 3.4 Detailed fabrication process of the device. (1-5) Starting with SOI wafer, deposition of SiO_2, bottom electrode, PZT, and patterning of top electrode by lift-off. (6-8) Patterning of PZT with wet etch, and bottom electrode and SiO_2 layers with RIE. (9-10) The front side silicon is shaped by DRIE, followed by the timed backside DRIE. (11-12) Final backside DRIE of Si and SiO_2 to release the device.

The front-side device structures are patterned and etched with deep reactive ion etch (DRIE) using the Bosch process (Mask 5). The backside is patterned with 10 μm of AZ 9260 resist (Mask 6) and is then time etched with DRIE. When 175 μm of Si has been etched from backside using DRIE, the remaining SiO_2 under the mirror is removed with dry etch. After completing the backside DRIE of Si the devices are released by the final oxide etch. This six mask fabrication scheme leaves oxide on the mirror, leading to somewhat increased stress. The oxide could easily be removed by adding one additional mask to the process. Details on the impact of this choice can be found in section 3.4.4.

3.3 Finite-Element Analysis

Finite-element analysis (FEA) of the PZT scanner is performed using ANSYS software. For the sake of simplicity only Si and PZT layers are modelled. Material properties are used as in Tab. 3.1.

Parameter	**PZT**	**Si**
Density ρ (kg/m^3)	7500	2330
C_{11} (10^9 N/m^2)	127	166.1
C_{12} (10^9 N/m^2)	80.2	64.2
C_{13} (10^9 N/m^2)	84.6	
C_{33} (10^9 N/m^2)	117	
C_{44} (10^9 N/m^2)	23	79.4
C_{55} (10^9 N/m^2)	23.4	
v	0.38	0.28

Table 3.1 Material Parameters Used for Modelling.

3.3.1 Modal Analysis

Modal analysis is done to extract the eigenmodes. As shown in Fig. 3.5, at the 2th mode, which is found to be at 15391 Hz, the outer frame and inner frame motions are in phase, and at 4th mode, which is found to be at 39579 Hz, the respective motions of the inner and the outer frame are out of phase. At the desired 4th mode, the mechanical coupling coefficient, which determines the rotation angle ratio of the outer frame and inner frame, is arranged to be 17.

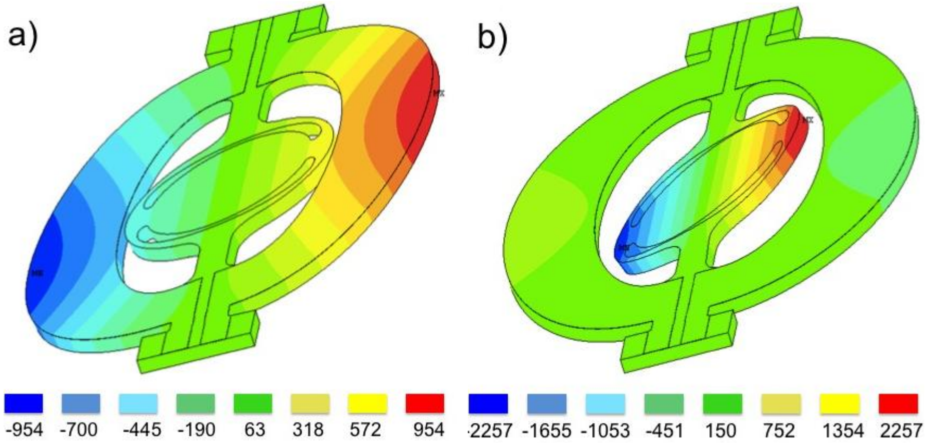

Figure 3.5 Shapes of the mechanical operation eigenmodes of the microscanner. The scales use an arbitrary unit. a) In-phase torsion mode where the outer frame and inner frame motions are in phase at 15391 Hz resonance frequency. b) Out-of-phase torsion mode where the outer frame and inner frame motions are out of phase with a rotation angle ratio of 17 at 39579 Hz resonance frequency.

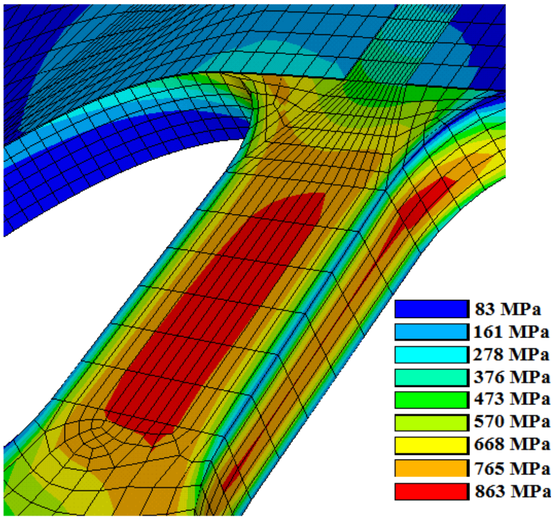

Figure 3.6 Stress distribution of the torsional scanner. At the desired mode of the scanner, stress is accumulated at the inner flexure, and the maximum principal stress is found to be 863 MPa at 10 deg. mechanical scan angle.

The dynamic deformation of the mirror is one of the essential properties of optical MEMS scanners that determine the quality of the reflected beam. Ideally it should be less than 10% of the longest utilized wavelength λ, the ultimate limit being 50% [76]. In this work the mirror is separated from the inner frame to decrease the effective stress on it and a stiffening backside rim is used support the mirror. The dynamic deformation along the mirror is calculated using the finite element model as shown in Fig. 3.7. About 2/3 of the mirror surface is usable for diffraction limited imaging as most of the deformation is near the edges. Note that while the maximum peak-to-valley dynamic deformation is 2.66 λ across the mirror, once the tilt is removed, the effective dynamic deformation will be about 0.45 λ = 230 nm (a factor of 6 reduction) according to the theory [11]. The acceptable level should be about 0.25 λ and can be achieved by further engineering of the backside stiffening rib.

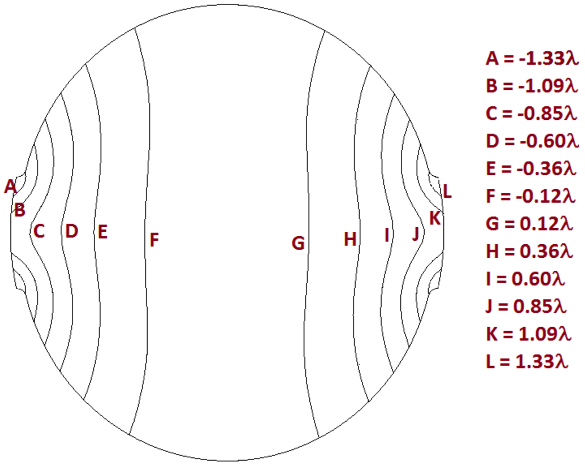

Figure 3.7 ANSYS analysis of the dynamical warping of the mirror at 10 deg. mechanical scan angle. The deformation amplitude is expressed in multiples of the wavelength λ = 510 nm.

3.4 Mechanical Characterization Results

3.4.1 Drive Characteristics

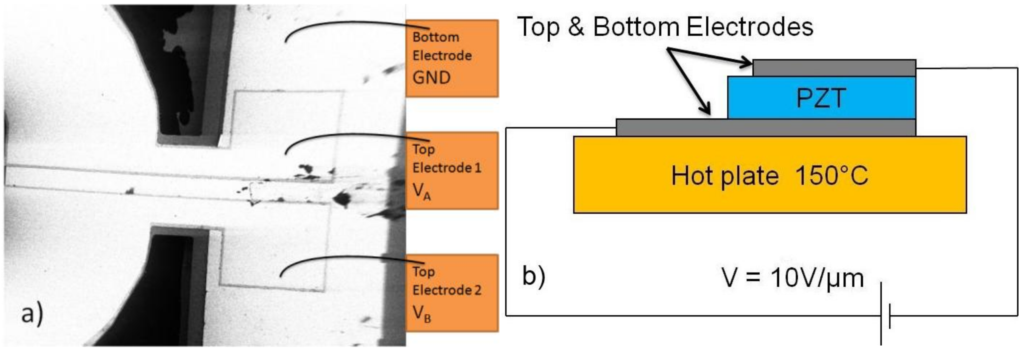

Figure 3.8 (a) SE micrograph of half of the device, showing the electrode orientation. (b) Sketch of a standard poling setup.

The device is divided into 3 isolated potentials, and electrical connections are achieved by wire bonding to the isolated areas as shown in Fig. 3.8a. Prior to any measurement, piezoelectric films were poled with 10 V µm^{-1} at an increased temperature of 150 C^{o}, for 15 min (Fig. 3.8b). All measurements referred in this paper are performed using the following dc-biased sinusoidal signals for device actuation to keep the polarity of the piezoelectric film in the correct direction.

$$V_A = \frac{V_0}{2}(1 + \sin \omega t) \tag{3.1}$$

$$V_B = \frac{V_0}{2}(1 - \sin \omega t) \tag{3.2}$$

where V_0 is the peak-to-peak (p-p) actuation voltage. These signals are applied to the electrodes placed on either side of the outer frame.

3.4.2 PZT Film Characterization

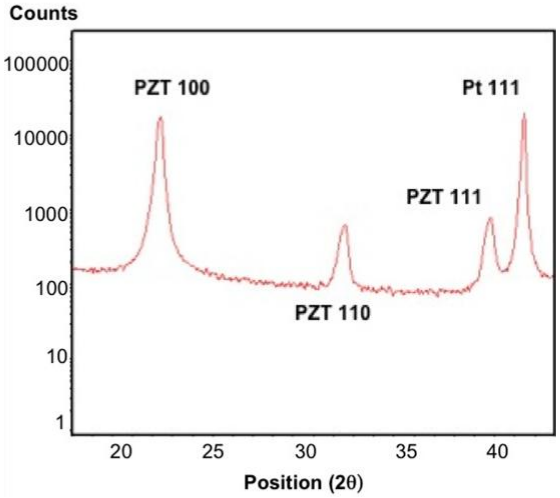

Figure 3.9 *θ-2θ* X-ray diffraction spectrum of the 2 μm thick PZT film

An X-ray diffraction measurement (Fig. 3.9) showed that the 2μm PZT film is (001)-textured to over 90%. The CV loop of the PZT capacitors (Fig. 3.10) shows typical ferroelectric characteristics with a peaking of the dielectric constant when domains are switching. PZT dielectric constant is extracted as 1200 at zero electric field. The dielectric constant is obtained by the usual relation:

$$\varepsilon_{PZT} = \frac{C \cdot t_{PZT}}{A \cdot \varepsilon_0} \tag{3.3}$$

where C is the capacitance, ε_0 is the vacuum dielectric constant, t_{PZT} is the thickness (2μm), and A is the area of the PZT film. The utilized sol-gel route for the PZT gives an $e_{31,f}$ piezoelectric coefficient from 12 to 14 C/m^2 and a d_{33} piezoelectric coefficient more than 100 pm/V [75, 77].

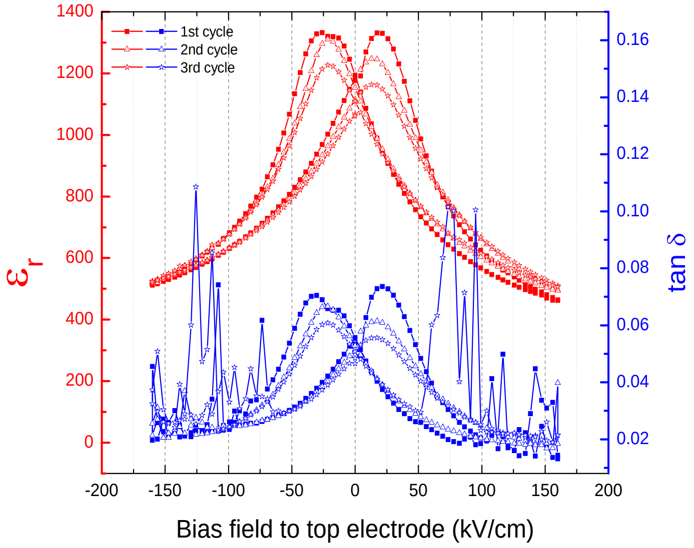

Figure 3.10 CV loops of the 2 μm thick PZT film.

3.4.3 Experimental Results

The PZT torsional scanner was tested to validate the mechanical-coupling mechanism under ambient pressure. The frequency response was measured at 7 V p-p actuation with laser doppler vibrometry (LDV) at the two measurement points shown in Fig. 3.3 to retrieve the motion of the outer frame and the mirror frame, respectively. For the mirror motion at the out-of-phase mode the LDV-data was corroborated with an angle measurement of a scanned laser spot. The mechanical response measured at the two points is presented in Fig. 8a as out-of-plane displacement. An actuation voltage of 7 V was used for the frequency response curves. In Fig. 3.11(b-c), the in-phase and the out-of-phase rotational modes (see Fig. 3.5) are presented in detail. For the two latter graphs the displacement is given as mechanical zero-to-peak (0-p) rotation. The frequency response shows, as expected, a slight spring stiffening effect. There are no jump discontinuities or measurable hysteresis.

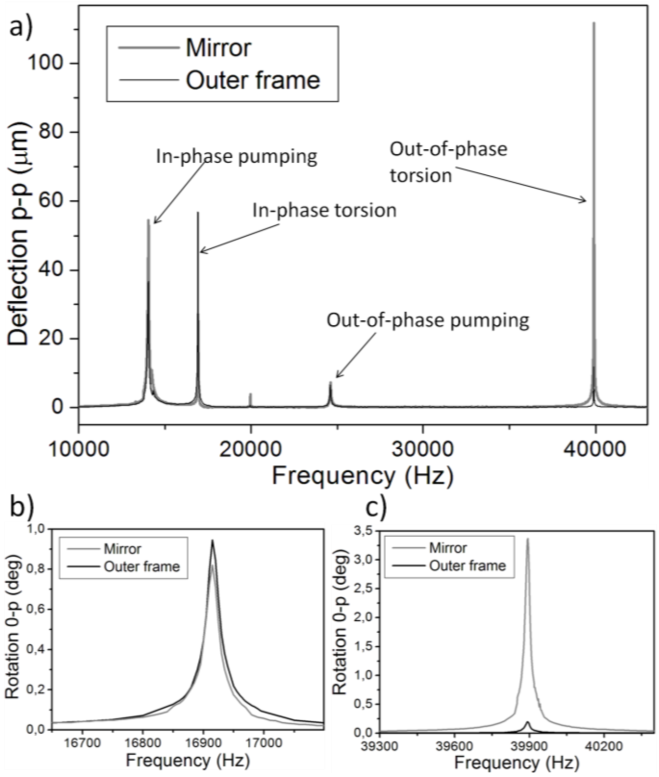

Figure 3.11 (a) Frequency response curve of a fabricated device while actuated with 7 V. The graph shows the vertical (out-of-plane) deflection as a function of frequency measured with LDV at the two points shown in Fig. 3.3. (b) In-phase torsion mode. To better illustrate the device behaviour the deflection is presented as

0-p rotation angle. (c) The out-of-phase torsion mode, which the device is designed for. The angular coupling factor between the frames is about 17.

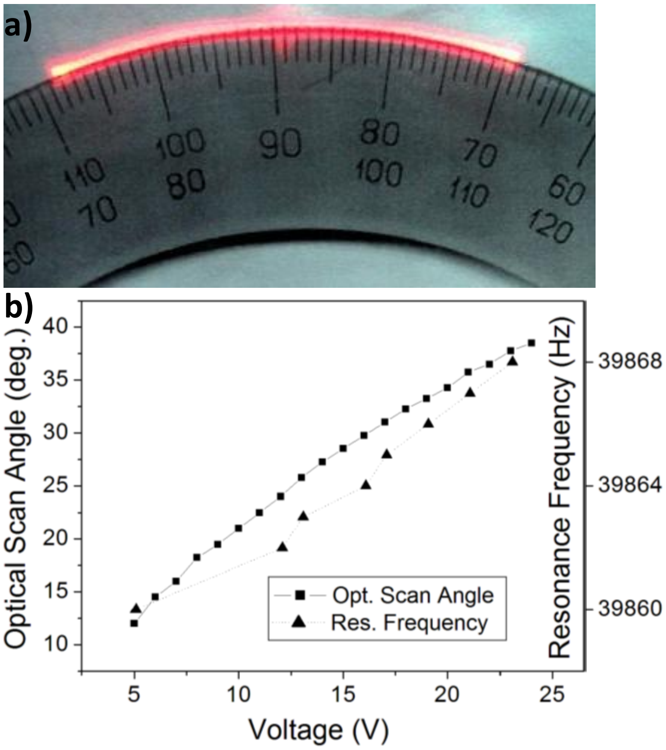

Figure 3.12 (a) The photograph shows a scanned beam with an optical angle of 38.5° at a drive voltage of 24 V. The curvature of the scanned beam is due to the incidence angle of the laser beam onto the mirror. This effect is utilized to measure the angle via the shown angle ruler. (b) Amplitude as a function of voltage at the resonance frequency. The frequency is adjusted in steps of 1 Hz at each voltage level to maximize the deflection. The angle ruler above is used for the measurement. The right hand y-axis shows the frequency shift for different voltages. A data point is put for each frequency increase. The frequency shift for the full sweep is only 0.02%.

The voltage response (Fig. 3.12b) was acquired by adjusting the actuation frequency to find the maximum response at each voltage level. The peak values for each voltage were measured using an angle measurer that is aligned with the corresponding scan line, as shown in Fig. 3.12a. The resonance frequency of the desired mode is around 39870 Hz, close to the FEM prediction. At V_0=24 V, an optical scan angle of 38.5 deg. is achieved for the D=1.4 mm mirror width. Corresponding to scanner comparison merits, the present scanner produces a $\theta_{OPT}\times D$ of 53.9 deg×mm at 40 kHz, leading to a $\theta_{OPT}\times D\times f$ of 2156 deg×mm×kHz. Although it is a high performing scanner, it consumes only about 28 mW as calculated from the equation provided in [78]

$$P = \omega \cdot C \cdot tan\delta \cdot V_0^2 \qquad \text{Equation 1}$$

where ω is the actuation frequency, C is the capacitance, $tan\delta$ is the loss factor, and V_0 is the root mean square of the actuation voltage.

At the out-of-phase torsion mode, the outer-frame deflection is amplified and transferred to the inner frame with a mechanical-coupling gain of about 17 and agrees well with the ANSYS simulation results.

3.4.4 Mirror Deformation Results

The static and dynamic deformations of the mirror were measured using a stroboscopic white light interferometer (Bruker, ContourGT In-Motion). As explained above, 2-μm-thick oxide is left below the mirror metal to shorten the fabrication process. The p-p static deformation of about 0.13 μm induced by the oxide is shown in Fig. 3.13. The static deformation can be eliminated by removing the oxide layer. The dynamic deformation of the mirror due to acceleration forces is calculated by subtracting the static deformation from the measured dynamic deformation at 4° mechanical angle (16° optical scan angle). As shown in Fig. 3.14, the p-p dynamic deformation is about 130 nm. At larger scan angles, fringes are blurred and the data is noisier. Since the deformation is linear with the scan angle, the dynamic deformation can be estimated as 325 nm at 10° mechanical angle, which agrees reasonably well with the 230 nm estimation using the FEM model.

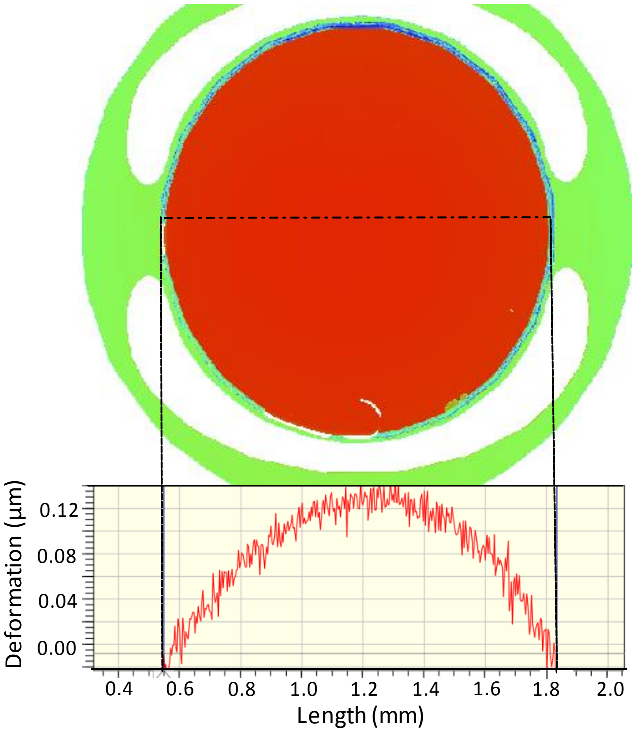

Figure 3.13. White light interferometer measurement of the mirror at rest.

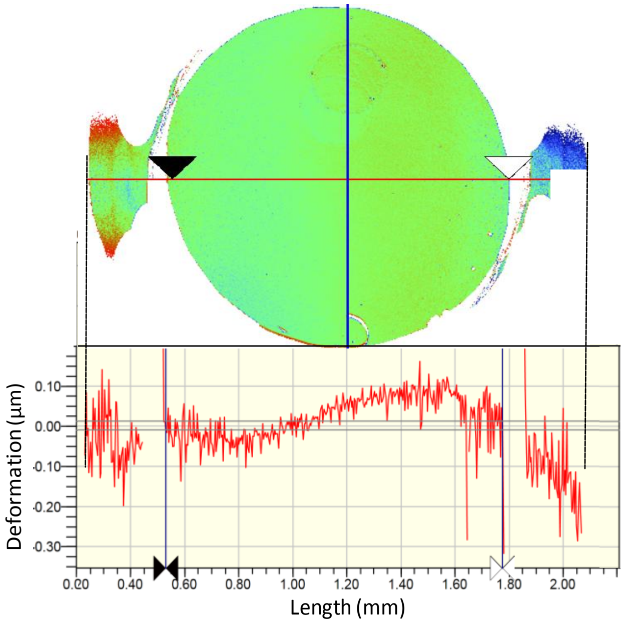

Figure 3.14 Dynamic deformation calculated by subtracting the mirror curvature at rest from the measured shape at 16° optical scan angle. The optically relevant p-p deformation is about 130 nm.

3.4.5 Angle Sensor Results

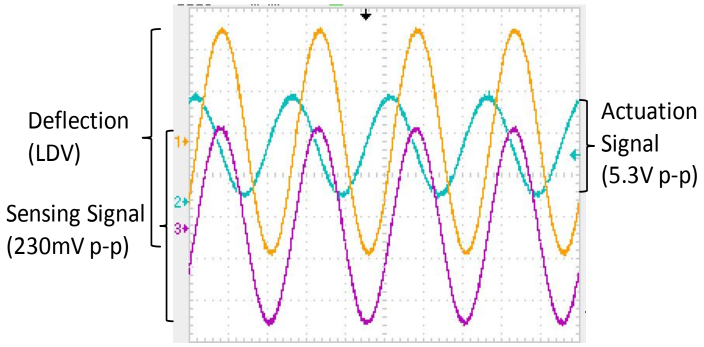

Figure 3.15 Example of the sensing signal while the device is vibrating at resonance with a mechanical zero-to-peak torsion angle of 1.6°. The device used for this experiment has segmented electrodes and only one fourth of the total PZT area is used for actuation, one fourth is used for sensing.

Since the phase is very sensitive close to resonance, a repeatable scan line requires angle feedback to meet the demands of dynamic displays. A version of the PZT where each sides of the PZT is segmented into two separate electrodes was fabricated to test the angle sensor concept. One half of the electrode in each side is used to drive the scanner and the other half is used for the scan angle sensing. Proof of concept experimental results are shown in Fig. 3.15.

The readout signal is very clear and at 230mV level. The sensing signal is 4.3% of the input voltage, which translates into very good conversion efficiency from the electrical to mechanical and back to electrical energy domain. The phase of the sensing signal follows the deflection signal measured with an LDV fully, with a constant small phase shift. PZT is generally known to have some hysteresis; however, since the stress on the film is bidirectional and symmetrical, the sensor signal is also bidirectional and doesn’t show any hysteresis. Future work will focus on engineering the size and location of the PZT angle sensor across the scanner to minimize the impact on actuator area.

3.5 Summary

A high performance PZT resonant scanner is designed, fabricated, and tested. A novel MEMS scanner solution, combining the mechanical coupling principle and PZT thin film actuation is proposed to achieve large optical angles at high frequencies. This way, optical rotation angle of 38.5 deg. is achieved with 1.4 mm mirror which operates with 24 V at 40 kHz resonance. Considering its rotation angle capability at a high frequency operation, it is a significant step towards achieving 1080p resolution with laser based mobile display.

4 CONCLUSIONS

This thesis reports design, simulation, fabrication and characterization results of two different scanners: first one is an electrostatically actuated non-resonant MEMS rotary stage designed to operate at 60Hz, and the second one is a piezoelectric actuated resonant MEMS torsion mirror designed to operate at high-frequencies.

Firstly, a MEMS rotary stage featuring a bending flexure suspension with linear stiffness is introduced. The stiffness linearity is demonstrated by the insignificant shift in the resonance frequency of the rotational mode with increased angle and by the linear relation between rotational angle and voltage up to ±7 deg. motion at resonance. The device is intended to be actuated quasi-statically at 60 Hz to enable its use as the slow-axis scanner for laser projection systems. However, pull-in that occurred at 40V, earlier than our prediction, prevented us from demonstrating the desired static rotation. Rotational asymmetry observed during the experiments can be considered as the major factor that led the comb fingers to an early pull-in. Future work should tackle this problem by making the second and third torsion resonant modes very close to each other, and having a thicker comb fingers. On the other hand, piezoelectric actuation is currently being exploited as an alternative to comb actuation for slow-axis scanner development.

Secondly, a high performance PZT resonant MEMS laser scanner is developed as a fast-axis component of a two-mirror micro-display system. A novel MEMS scanner solution, combining the mechanical coupling principle and PZT thin film actuation is proposed to achieve large optical angles at high frequencies. Analytical reasoning and a finite-element-model is developed and validated with experimental results. The present scanner is the highest performing in the current literature in terms of the product of mirror size (1.4 mm), optical scan angle (38.5°), and resonance frequency 39,870 Hz. In addition to this record performance, it consumes only about 28 mW power, which is little compared with other actuation schemes. Dynamic deformation of the mirror is taken under control by separating it from the inner frame and using backside reinforcement rim underneath the mirror. Moreover, preliminary PZT sensing experiments are done by separating PZT layers for actuation and sensing purposes.

The presented scanner's performance meets the frequency requirements and with further work will be able to meet all the requirements of full HD resolution pico-projectors.

BIBLIOGRAPHY

[1] A. Korpel, *et al.*, "A television display using acoustic deflection and modulation of coherent light," *Applied Optics,* vol. 5, pp. 1667-1675, 1966.

[2] K. V. Chellappan, *et al.*, "Laser-based displays: a review," *Applied Optics,* vol. 49, pp. F79-F98, 2010.

[3] S. J. Park, *et al.*, "Design considerations for pico-projector based on LCoS and 3-LEDs," 2011, pp. 805-806.

[4] M. Leddy, *et al.*, "Digital micro-mirror based image simulation system," ed: Google Patents, 1995.

[5] P. Janssens, *et al.*, "9.3: LCoS Laser Projector."

[6] S. C. Shin, *et al.*, "The Compact Systems Design Based on DMD and the Straight Line 2-Channel LED for a Mobile Embedded Pico Projector," *Journal of Display Technology,* vol. 8, pp. 219-224, 2012.

[7] D. Raboud, *et al.*, "MEMS based color-VGA micro-projector system," *Procedia Engineering,* vol. 5, pp. 260-263, 2010.

[8] M. Freeman, *et al.*, "Scanned laser pico-projectors: Seeing the big picture (with a small device)," *Optics and Photonics News,* vol. 20, pp. 28-34, 2009.

[9] A. D. Yalcinkaya, *et al.*, "Two-axis electromagnetic microscanner for high resolution displays," *Microelectromechanical Systems, Journal of,* vol. 15, pp. 786-794, 2006.

[10] H. Urey, "Torsional MEMS scanner design for high-resolution display systems," 2002, pp. 27-37.

[11] H. Urey, *et al.*, "Optical performance requirements for MEMS-scanner based microdisplays," 2000, pp. 176-185.

[12] J. Tauscher, *et al.*, "Evolution of MEMS scanning mirrors for laser projection in compact consumer electronics," 2010, p. 75940A.

[13] R. B. Sprague, *et al.*, "Bi-axial magnetic drive for scanned beam display mirrors," 2005, p. 1.

[14] E. S. Hung and S. D. Senturia, "Extending the travel range of analog-tuned electrostatic actuators," *Microelectromechanical Systems, Journal of,* vol. 8, pp. 497-505, 1999.

[15] H. Urey, "MEMS scanners for display and imaging applications," 2004, p. 219.

[16] K. Uchino, "Piezoelectric actuators 2006," *Journal of Electroceramics,* vol. 20, pp. 301-311, 2008.

[17] P. Muralt, "Piezoelectric thin films for MEMS," *Integrated Ferroelectrics,* vol. 17, pp. 297-307, 1997.

[18] U. Baran, *et al.*, "A Built-in Vibration Sensor Using Arc-Discharged Reactive Ion Plated PZT," *IEEJ,* vol. 131, pp. 128-129, 2011.

[19] C. Lee, *et al.*, "Development of a piezoelectric self-excitation and self-detection mechanism in PZT microcantilevers for dynamic scanning force microscopy in liquid," *Journal of Vacuum Science & Technology B: Microelectronics and Nanometer Structures,* vol. 15, p. 1559, 1997.

[20] H. Miyajima, *et al.*, "A durable, shock-resistant electromagnetic optical scanner with polyimide-based hinges," *Microelectromechanical Systems, Journal of,* vol. 10, pp. 418-424, 2001.

[21] G. Reyne, "Electromagnetic actuation for MOEMS, examples, advantages and drawbacks of MAGMAS," *Journal of magnetism and magnetic materials,* vol. 242, pp. 1119-1125, 2002.

[22] J. Kim and L. Lin, "Electrostatic scanning micromirrors using localized plastic deformation of silicon," *Journal of Micromechanics and Microengineering,* vol. 15, p. 1777, 2005.

[23] J. W. Cho, *et al.*, "Electrostatic 1D microscanner with vertical combs for HD resolution display," 2007, p. 64660B.

[24] Y. C. Ko, *et al.*, "Eye-type scanning mirror with dual vertical combs for laser display," *Sensors and Actuators A: Physical,* vol. 126, pp. 218-226, 2006.

[25] M. Yoda, *et al.*, "A MEMS 1D optical scanner for laser projection display using self-assembled vertical combs and scan-angle magnifying mechanism," 2005, pp. 968-971 Vol. 1.

[26] A. Arslan, *et al.*, "Comb-Actuated Resonant Torsional Microscanner With Mechanical Amplification," *Microelectromechanical Systems, Journal of,* vol. 19, pp. 936-943, 2010.

[27] S. K. Gokce, *et al.*, "A high-frequency comb-actuated resonant MEMS scanner for microdisplays," 2011, pp. 35-36.

[28] T. Sandner, *et al.*, "Damping analysis and measurement for a comb-drive scanning mirror," 2004, p. 147.

[29] J. G. Smits, *et al.*, "Microelectromechanical flexure PZT actuated optical scanner: static and resonance behavior," *Journal of Micromechanics and Microengineering,* vol. 15, p. 1285, 2005.

[30] F. Filhol, *et al.*, "Resonant micro-mirror excited by a thin-film piezoelectric actuator for fast optical beam scanning," *Sensors and Actuators A: Physical,* vol. 123, pp. 483-489, 2005.

[31] J. H. Park, *et al.*, "High-speed metal-based optical microscanners using stainless-steel substrate and piezoelectric thick films prepared by aerosol deposition method," *Sensors and Actuators A: Physical,* vol. 135, pp. 86-91, 2007.

[32] S. Matsushita, *et al.*, "Metal-based piezoelectric microelectromechanical systems scanner composed of Pb (Zr, Ti) O 3 thin film on titanium substrate," *Microsystem Technologies*, pp. 1-7.

[33] T. Iseki, *et al.*, "High-Speed and Wide-Angle Deflection Optical MEMS Scanner Using Piezoelectric Actuation," *IEEJ Transactions on Electrical and Electronic Engineering,* vol. 5, pp. 361-368, 2010.

[34] A. D. Yalcinkaya, *et al.*, "NiFe plated biaxial MEMS scanner for 2-D imaging," *Photonics Technology Letters, IEEE,* vol. 19, pp. 330-332, 2007.

[35] H. M. Jeong, *et al.*, "Slow scanning electromagnetic scanner for laser display (Journal Paper)," 2008.

[36] W. Makishi, *et al.*, "Magnetic torque driving 2D micro scanner with a non-resonant large scan angle," 2009, pp. 904-907.

[37] H. Schenk, *et al.*, "Large deflection micromechanical scanning mirrors for linear scans and pattern generation," *Selected Topics in Quantum Electronics, IEEE Journal of,* vol. 6, pp. 715-722, 2000.

[38] W. Piyawattanametha, *et al.*, "Surface-and bulk-micromachined two-dimensional scanner driven by angular vertical comb actuators," *Microelectromechanical Systems, Journal of,* vol. 14, pp. 1329-1338, 2005.

[39] I. W. Jung, *et al.*, "High fill-factor two-axis gimbaled tip-tilt-piston micromirror array actuated by self-aligned vertical electrostatic combdrives," *Microelectromechanical Systems, Journal of,* vol. 15, pp. 563-571, 2006.

[40] D. W. Wine, *et al.*, "Performance of a biaxial MEMS-based scanner for microdisplay applications," 2000, pp. 186-196.

[41] V. Milanovic, *et al.*, "Gimbal-less monolithic silicon actuators for tip-tilt-piston micromirror applications," *Selected Topics in Quantum Electronics, IEEE Journal of,* vol. 10, pp. 462-471, 2004.

[42] Y. Du, *et al.*, "A 2-DOF circular-resonator-driven in-plane vibratory grating laser scanner," *Microelectromechanical Systems, Journal of,* vol. 18, pp. 892-904, 2009.

[43] U. Baran, *et al.*, "Linear-Stiffness Rotary MEMS Stage," *Microelectromechanical Systems, Journal of,* pp. 1-3.

[44] M. Tani, *et al.*, "A two-axis piezoelectric tilting micromirror with a newly developed PZT-meandering actuator," 2007, pp. 699-702.

[45] M. Tani, *et al.*, "A combination of fast resonant mode and slow static deflection of soi-pzt actuators for mems image projection display," 2006, pp. 25-26.

[46] T. Kobayashi, *et al.*, "Low speed piezoelectric optical microscanner actuated by piezoelectric microcantilevers using LaNiO3 buffered Pb (Zr, Ti) O3 thin film," *Smart Materials and Structures,* vol. 18, p. 065008, 2009.

[47] C. H. Ji, *et al.*, "Electromagnetic two-dimensional scanner using radial magnetic field," *Microelectromechanical Systems, Journal of,* vol. 16, pp. 989-996, 2007.

[48] S. Hsu, *et al.*, "Fabrication and characterization of a dynamically flat high resolution micro-scanner," *Journal of Optics A: Pure and Applied Optics,* vol. 10, p. 044005, 2008.

[49] T. Sandner, *et al.*, "Microscanner with vertical out of plane combdrive," 2011, pp. 33-34.

[50] H. Schenk, *et al.*, "A resonantly excited 2D-micro-scanning-mirror with large deflection," *Sensors and Actuators A: Physical,* vol. 89, pp. 104-111, 2001.

[51] D. Kallweit, *et al.*, "Fabrication of a quasistatic-resonant microscanner by implementing a vertical combdrive through wafer assembly actuation," 2011, pp. 147-148.

[52] H. M. Chu and K. Hane, "Design, fabrication and vacuum operation characteristics of two-dimensional comb-drive micro-scanner," *Sensors and Actuators A: Physical,* vol. 165, pp. 422-430, 2011.

[53] Y. Yasuda, *et al.*, "Piezoelectric 2D-optical micro scanners with PZT thick films," *Integrated Ferroelectrics,* vol. 80, pp. 341-353, 2006.

[54] M. Tani, *et al.*, "A laser display using a PZT-actuated 2D optical scanner," 2005, pp. 9-10.

[55] J. Tsaur, *et al.*, "2D micro scanner actuated by sol-gel derived double layered PZT," 2002, pp. 548-551.

[56] T. Juneau, *et al.*, "Dual axis operation of a micromachined rate gyroscope," 1997, pp. 883-886 vol. 2.

[57] T. Fujita, *et al.*, "Disk-shaped bulk micromachined gyroscope with vacuum sealing," *Sensors and Actuators A: Physical,* vol. 82, pp. 198-204, 2000.

[58] J. D. Grade, *et al.*, "Advanced, vibration-resistant, comb-drive actuators for use in a tunable laser source," *Sensors and Actuators A: Physical,* vol. 114, pp. 413-422, 2004.

[59] J. Grade and H. Jerman, "MEMS electrostatic actuators for optical switching applications," 2001.

[60] J. A. Yeh, *et al.*, "MOEMS variable optical attenuators using rotary comb drive actuators," *Photonics Technology Letters, IEEE,* vol. 18, pp. 1170-1172, 2006.

[61] T. C. Leïchlé, *et al.*, "A low-power resonant micromachined compass," *Journal of Micromechanics and Microengineering,* vol. 14, p. 462, 2004.

[62] W. O. Davis, *et al.*, "On the nonlinear dynamics of tether suspensions for MEMS," *Journal of vibration and acoustics,* vol. 126, pp. 326-331, 2004.

[63] J. A. Yeh, *et al.*, "Large rotation actuated by in-plane rotary comb-drives with serpentine spring suspension," *Journal of Micromechanics and Microengineering,* vol. 15, p. 201, 2005.

[64] A. H. Nayfeh, *et al.*, "Nonlinear Oscillations," *Journal of Applied Mechanics,* vol. 47, p. 692, 1980.

[65] M. Stranczl, *et al.*, "High-Angular-Range Electrostatic Rotary Stepper Micromotors Fabricated With SOI Technology," *JOURNAL OF MICROELECTROMECHANICAL SYSTEMS,* vol. 21, p. 605, 2012.

[66] W. Davis, *et al.*, "Nonlinear elastic coupling in tether-suspended MEMS," pp. 129-132.

[67] J. Bronson and I. Fassi, "Parametric design of an electrostatic rotary microactuator using finite element analysis and metamodeling," 2008, pp. 1-8.

[68] W. O. Davis, *et al.*, "High-performance silicon scanning mirror for laser printing," 2007, p. 64660D.

[69] T. Iseki, *et al.*, "Shrinking design of a MEMS optical scanner having four torsion beams and arms," *Sensors and Actuators A: Physical,* vol. 164, pp. 95-106, 2010.

[70] K. Yamada and T. Kuriyama, "A novel asymmetric silicon micro-mirror for optical beam scanning display," 1998, pp. 110-115.

[71] M. Lebedev, *et al.*, "Optical micro-scanner fabricated on stainless steel by aerosol deposition method," 2004, pp. 165-168.

[72] S. Matsushita, *et al.*, "Metal-based piezoelectric MEMS scanner mirrors composed of PZT thin films on titanium substrates," 2011, pp. 574-577.

[73] D. B. Utku Baran, Sven Holmstrom, Davide Balma, Wyatt Davis, Paul Muralt, Hakan Urey, "High Frequency Torsional MEMS Scanner for Displays," in *IEEE MEMS*, Paris, 2012.

[74] P. Muralt, *et al.*, "Texture control of PbTiO and Pb (Zr, Ti) O thin films with TiO seeding," *Journal of applied physics,* vol. 83, p. 3835, 1998.

[75] F. Calame and P. Muralt, "Growth and properties of gradient free sol-gel lead zirconate titanate thin films," *Applied physics letters,* vol. 90, p. 062907, 2007.

[76] H. Urey and D. L. Dickensheets, "Display and Imaging systems," *MOEMS and Applications*, 2005.

[77] N. Ledermann, *et al.*, "{1 0 0}-Textured, piezoelectric Pb (Zrx, Ti1-x) O3 thin films for MEMS: integration, deposition and properties," *Sensors and Actuators A: Physical,* vol. 105, pp. 162-170, 2003.

[78] N. G. Ledermann, "Piezoelectric Acoustic Sensors and Ultrasonic Transducers Based on Textured PZT Thin Films," ÉCOLE POLYTECHNIQUE FÉDÉRALE DE LAUSANNE, 2003.

VITA

Utku Baran was born in Ankara, Turkey, in 1987. He received his B.Sc. degree in Electrical and Electronics Engineering (with high merit scholarship) from Koç University, Istanbul, Turkey, in 2010. Since then, he has been working at Optical Microsystems Laboratory (OML) of Koç University, Department of Electrical Engineering as a M.Sc. candidate.

He worked as an undergraduate research assistant at OML for three years, and has been in Microvision Inc., University of Tokyo, NC State University, and Aselsan as an intern. He also spent 4 months at EPFL-Switzerland as a visiting researcher.

He is the author of more than 6 journal and conference papers, and the co-inventor of 2 pending US patents.